International Journal of Hydrogen Energy 163 (2025) 150728

Contents lists available at ScienceDirect

International Journal of Hydrogen Energy

journal homepage: www.elsevier.com/locate/he

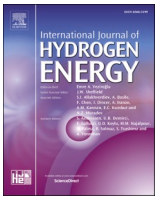

# Valorized S/N-doped banana peel biochar as a sustainable OER electrocatalyst for green energy applications

Silvia Escudero-Curiel [a,b,*], Aida M. Díez [a,**], Marta Pazos [a], Ángeles Sanromán [a]

[a] CINTECX, Universidade de Vigo, Department of Chemical Engineering. Campus As Lagoas-Marcosende, 36310, Vigo, Spain
[b] Department of Chemical Engineering, Imperial College London, London, SW7 2AZ, UK

ARTICLE INFO

Handling Editor: Dr Mehran Rezaei

*Keywords:*
Biochar electrocatalyst
Co-doping
Water splitting
Hydrogen production
Sustainable energy
Circular economy

ABSTRACT

Decarbonization necessitates innovative energy solutions, such as $H_2$ production through water splitting reactions, which critically relies on efficient catalysts to enhance both efficiency and cost-effectiveness. Employing carbocatalysts synthesized from agro-industrial residues and co-doped with nitrogen and sulfur represents a groundbreaking strategy that not only supports decarbonization efforts but also accelerates the transition towards a circular economy model. In this study, we have developed a novel oxygen evolution reaction (OER) eco-electrocatalyst by doping banana peel-derived biochar with varying levels of thiourea. The optimal eco-electrocatalyst, 5 %-S/N@BC, significantly surpasses the efficiency of $IrO_2$ and outperforms many reported carbon-based electrodes in terms of initial performance and long-term stability. Notably, it achieves overpotentials of 290, 322, and 334 mV at current densities of 10, 50, and 100 mA $cm^{-2}$, respectively, over 30-h periods. The process has been optimized regarding pH, catalyst dose, and dopant concentration. Furthermore, the eco-electrocatalyst demonstrates a competitive overall water splitting behavior, attaining a notably low cell voltage of 1.58 V required for reaching 10 mA $cm^{-2}$. Comprehensive characterization using FTIR, Raman, XRD, XPS, and SEM-EDS have been conducted to validate these findings. This represents the first demonstration of a metal-free S/N@BC catalyst derived from banana peel for efficient OER. Our research highlights the significance of avoiding precious and transition metals, as well as the value of creating carbon-based catalysts fully sourced from biomass. The development of such materials plays a crucial role in advancing sustainable catalyst design while fostering a circular economy through the effective utilization of agro-industrial waste. Furthermore, only a limited number of studies have focused solely on biomass-derived materials, and among those, their catalytic performance rarely exceeds the results demonstrated in this work.

## 1. Introduction

Recommendations have been made to use alternative energy sources to advance towards decarbonization. Hydrogen ($H_2$) production has emerged as a viable alternative energy solution with multiple production pathways, conventionally classified as grey, blue, and green $H_2$ [1]. Current industrial $H_2$ generation remains predominantly dependent on fossil fuel-based methods (grey and blue variants), which continue to significantly contribute to global greenhouse gas emissions [2]. Water electrolysis (water splitting) represents one of the most sustainable methods for green $H_2$ production, offering a viable alternative to conventional fossil fuel-based generation. This approach facilitates the direct use of renewable energy sources while ensuring completely carbon-free operation, as it generates zero $CO_2$ emissions during the $H_2$ synthesis process [3]. This process involves two key reactions: water reduction, known as the Hydrogen Evolution Reaction (HER), and water oxidation, termed the Oxygen Evolution Reaction (OER). OER is a critical bottleneck due to its inherently sluggish kinetics, which arise from the complex four-proton-coupled electron transfer mechanism required for water oxidation [4]. The overall mechanism involved is shown in equations (1)–(4) [5], where * represents the catalyst's active site, (g) and (l) indicate the gas and liquid phase respectively, and *OH, *O, *OOH denote adsorbed species on the catalyst. Electrocatalysts design faces significant challenge in this process trying to reduce the overpotential required to drive these reactions efficiently beyond its thermodynamic value. Minimizing this excess potential remains a central

* Corresponding author.
** Corresponding author.
*E-mail addresses:* sescudero@uvigo.gal (S. Escudero-Curiel), adiez@uvigo.gal (A.M. Díez).

https://doi.org/10.1016/j.ijhydene.2025.150728
Received 21 May 2025; Received in revised form 15 July 2025; Accepted 27 July 2025
Available online 5 August 2025

challenge in advancing sustainable electrochemical technologies. Currently, costly and scarce Pt/C and $IrO_2$ serve as standard catalysts for HER and OER respectively [6,7], but their commercial viability is hindered by limited stability under high oxidative potentials at low pH [8]. Moreover, precious metal extraction and recovery severely pollute ecosystems at high environmental costs [9]. Hence, this drives the need to find affordable, high performing substitutes for these precious metals that could reduce overpotential, provide active sites that stabilize critical intermediates (e.g., *O, *OH, *OOH) and lower activation barriers [10].

$$* + OH^- \rightarrow *OH + e^- \quad \text{(Eq. 1)}$$

$$*OH + OH^- \rightarrow *O + H_2O(l) + e^- \quad \text{(Eq. 2)}$$

$$*O + OH^- \rightarrow *OOH + e^- \quad \text{(Eq. 3)}$$

$$*OOH + OH^- \rightarrow * + O_2(g) + H_2O(l) + e^- \quad \text{(Eq. 4)}$$

Concurrently, recent data shows global agricultural activities yield about 1 billion tons of residues annually, contributing roughly 20 % of greenhouse gas emissions [11]. Residues stem from challenges in harvesting, storage, transport, processing, and marketing, notably in small to medium-scale sectors [12]. The rapid expansion of agriculture and the increasing demand for its products are placing significant stress on the environment, climate, ecosystems, and health [13]. Agricultural production needs a 50 % boost by 2050 to meet a projected 12 billion tons demand, driven by an expected 8.5 billion population by 2030 [14]. Furthermore, these projected population growth figures will accentuate the energy supply problem, as they are currently based on non-renewable sources, primarily fossil fuels [15]. According to the above, the United Nations urges to reduce fossil fuel use and transitioning toward Zero Waste principles [16].

Within this framework, a holistic solution using agricultural residues as the basis for green and renewable energy solutions is proposed in this study. Carbon-based catalysts not only hold potential for substituting metallic catalysts but also provide an opportunity to contribute to sustainable production and Zero Waste principles [17]. Ecological OER-carbocatalysts can be obtained through thermochemical conversion processes like dry or wet pyrolysis to yield biochar or hydrochar respectively, utilizing agricultural residues, particularly biomass rich in lignocellulosic components [18]. These eco-electrocatalyst have proven to be stable even in the OER potential range in alkaline conditions [4]. While pristine chars typically exhibit lower catalytic activity compared to metallic counterparts, they offer a customizable surface that allows adjustment of their electronic and physicochemical properties [19,20]. Tailoring chars aims to enhance their suitability for catalytic applications [21]. Some carbon-based catalysts have been utilized as OER-catalysts, but they have typically been enhanced through metal doping, such as Zn(O,S) [22], molybdenum [23] or cobalt [24]. Alternatively, incorporation of heteroatoms, particularly N, S and P, into the carbon lattice disturbs the initial surface charge balance and induces bond polarization at the insertion point [25], resulting in a more conducive material that promotes electron transfer mechanisms that initiate various electro-activation pathways [26]. Conventional methods of introducing N and S into the carbon matrix involve blending precursors of both elements before or after pyrolysis [27] or by ammonia gas treatment [28]. However, strong acid or alkaline treatments are typically carried out before or after pyrolysis to complete the treatment process [29,30]. Previous authors have essayed the one pot synthesis of thiourea-based biochar from nanocellulose although for other catalytic uses, demonstrating the usefulness of S/N doping for the increase of catalytic active sites [31]. Thus, it is reasonable to expect an enhanced water splitting activity with S/N doped biochars.

Therefore, this study aims to valorize banana peel, an abundant agricultural residue sourced from a local food-processing company, as an OER-catalyst by transforming it into S/N co-doped biochar (S/N@BC) via a greener and controllable one-pot grafting process using thiourea as an eco-friendly doping agent. To our knowledge, this is the first instance of using a S/N@BC derived from banana peel as OER-catalyst without additional metals supplement. Our study underscores not only the relevance of eliminating the use of precious and transition metals, but also the importance of developing carbon-based catalysts entirely derived from biomass. Advancing such materials contributes significantly to sustainable catalyst design while promoting a circular economy through the valorization of agro-industrial residues. Moreover, only a few studies using exclusively biomass-derived materials have been reported, and when they have, their performance has rarely surpassed that achieved in the present work [25,32–34].

## 2. Experimental section/methods

### 2.1. Catalyst synthesis

Banana peels were kindly provided by Freshcut S.L (Pontevedra, ESP), dried at 60 °C overnight and ground afterwards. Banana peel biochar (BC) was synthesized at a pyrolysis temperature of 550 °C for 4 h in a tubular furnace (Carbolite Gero, DEU), with a heating ramp of 5 °C $min^{-1}$ and a $N_2$ flow of 300 mL $min^{-1}$. The co-doping process was carried out in a one-step by a one-pot synthesis where both banana peels and the co-doping agent were added to the tubular furnace. Various levels of thiourea (99.6 %, VWR) were used for synthesizing S/N@BC, with weight percentages relative to the raw banana peel being 2.5 %, 5 %, and 10 %. The resulting samples were named as follows: 2.5 %-S/N@BC, 5 %-S/N@BC and 10 %-S/N@BC. Urea (99 %, Sigma-Aldrich) was used to obtain N-doped sample 5 %-N@BC following the same doping process.

Eco-electrodes were prepared following Díez et al. [35] procedure. Briefly, 5 mg of S/N@BC was mixed with 50 μL of a 5 % conductive Nafion® ionomer solution in aliphatic alcohols and water (80 %, Sigma Aldrich), and 1 mL of ethanol (99.5 %, Scharlab). This mixture was subjected to ultrasonic dispersion (37 kHz, 150 W, Bandelin Sonopuls sonicator) for 2 min, followed by vortex mixing (Vortex-Genie® 2 mixer) to obtain a uniform suspension. The resulting ink was then applied to a 1 cm × 1 cm piece of nickel foam, using 20 μL increments until the desired catalyst loading was obtained. Hot air was used to promote solvent evaporation between applications, ensuring the electrocatalyst evenly covered the foam's surface area. Likewise, the reference Pt–C/$IrO_2$ (99.9 %, Alfa-Aesar) was drop-deposited at a total of 1 mg $cm^{-2}$. A detailed scheme of the catalysts synthesis is presented in Fig. 1.

### 2.2. Water splitting configuration

To assess the synthesized N/S@BC, a three-electrode configuration was set up (Fig. 2), interfaced with an Autolab potentiostat (Methrom), using Nova 2.1 Software for data collection. OER experiments were conducted at a pH of 14, using a 1 M NaOH solution (99 %, Sigma Aldrich), a pH of 6.64 in a 2 M $Na_2SO_4$ solution and a pH 0.29 in a 0.5 M $H_2SO_4$ solution. An Ag/AgCl electrode served as the reference, while a Pt wire (40 % Pt content, Alfa-Aesar) functioned as the counter electrode in alkaline media. The working electrode was Ni-foam (1 $cm^2$) initially cleaned with 30-min sonication baths in acetone (99 %, Sigma Aldrich), ethanol, and distilled water, then dried overnight at 60 °C. For acidic pH testing, carbon paper was employed as working electrode and a carbon stick served as counter electrode to prevent metal leaching.

### 2.3. Electrochemical measurements

The primary metric used to assess OER performance was CV. A potential window of 0–0.74 V, 0.48–1.2 V and 0.8–1.54 for, respectively, alkaline, neutral and acid pHs following the Nernst equation. This potential corresponds to the overpotential typically referenced in OER for $O_2$ generation (−1.23 V vs RHE). The scan rate was set at 0.05 mV $s^{-1}$.

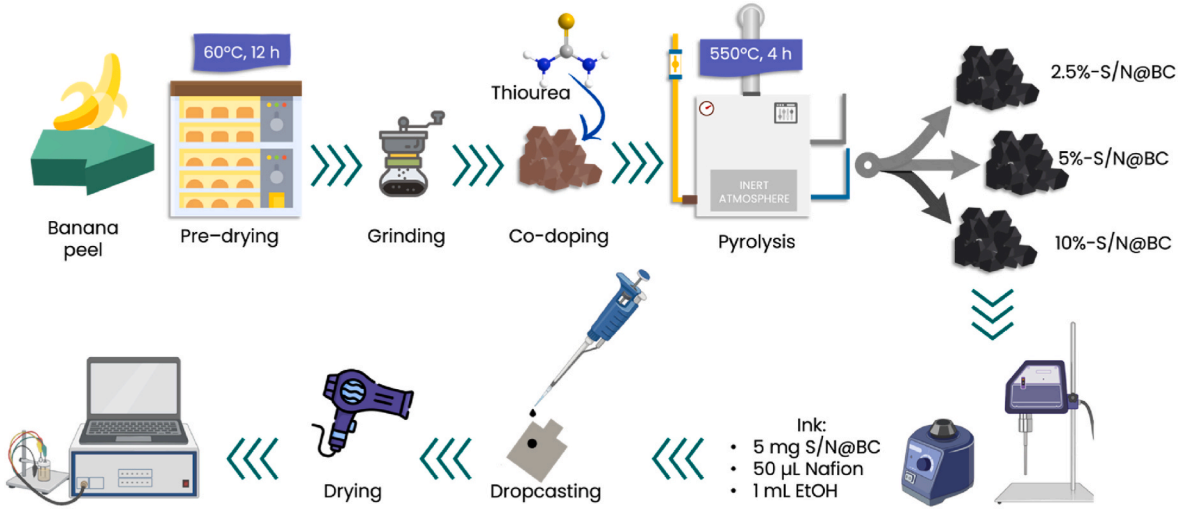


**Fig. 1.** Diagram of the one-step, one-pot synthesis and electrode preparation methods used in this study.

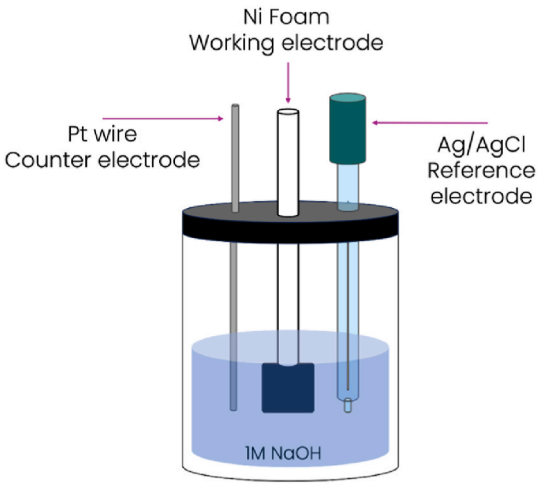


**Fig. 2.** Three-electrode cell setup used for water splitting measurements in the potentiostat.

From CV, Tafel Slope is attained by applying Eq. (5) where $\eta$ is the overpotential (V), $a$ the order at the origin, $b$ the Tafel slope (V dec$^{-1}$) and $j$ the applied current (A). This parameter provides information about the charge transfer kinetics [6]. For acidic HER evaluation, Linear Sweep Voltammetries (LSV) preventing catalyst oxidation were conducted and the potential window was set from −0.25 to −0.6 V.

$$\eta = a + b^{*}\log j \quad \text{(Eq. 5)}$$

To ensure the selected catalyst's long-term viability, stability tests were conducted. Chronopotentiometry and Accelerated Durability Tests (ADT) were employed for this purpose. Chronopotentiometry involved maintaining a constant current of 10, 50 and 100 mA cm$^{-2}$ for 30 h each while monitoring the corresponding potential. The smaller the variation in potential over time, the greater the catalyst's stability. ADT entailed subjecting the catalyst to 10,000 cyclic voltammetry scans, comparing the initial and final scans to assess material stability. Following stability testing, the catalyst was extracted from the electrode by immersing the catalytic electrode in 1.5 mL of ethanol and sonicating it with the tubular probe. Subsequently, the ethanol was evaporated to allow for the characterization of the used catalyst.

### 2.4. Electrochemical characterization

To determine the ECSA, measurements were taken over a 0.1 V range in the non-Faradaic region, with scan rates varying from 10 to 400 mV s$^{-1}$. The ECSA was calculated by plotting the scan rate against half the difference in current density between the anodic and cathodic sweeps, resulting in a linear relationship. The slope of this plot provided the geometric CDL. The ECSA was then determined using Eq. (6), where Cs, the specific capacitance, was set at 40 µF cm$^{-2}$ [7,14].

$$\mathrm{ECSA} = \mathrm{CDL}/_{\mathrm{Cs}} \quad \text{(Eq. 6)}$$

EIS was recorded within the frequency range of 0.1–10$^{5}$ Hz to evaluate charge transfer impedance, resulting in the Nyquist plot. The semi-circle observed in the Nyquist plot represents the charge transfer resistance (Rp), while the plot's origin (Rs) represents the system resistance, including the setup, electrolyte, and electrodes. By fitting the Nyquist plot to an equivalent circuit, these resistance parameters were extracted, enabling a comparison of catalytic performance in terms of Rp [36].

Electric efficiency was calculated at each current density according to the standard approach, as the ratio between the thermodynamic potential for water splitting (1.23 V) and the experimentally measured cell potential [37].

Both the synthesis and electrochemical characterization were performed in duplicate in this study. The results presented show the calculated averages. For greater clarity, the standard deviation (SD) is indicated next to the name of each series in the CV plots when more than 2 samples are represented.

### 2.5. Characterization

The Point of Zero Charge (PZC) was determined for all samples following Rosales et al. [38] procedure with some adjustments. Briefly, a series of five 0.1 M $NaNO_3$ solutions at various pH levels (ranging from 2 to 12) were prepared, with initial pH adjustments made using 1 M $HNO_3$ and 1 M NaOH. After 24 h, the final pH of the supernatant was measured using a Hach-Lange SensIon + PH3 pH-meter.

Further characterization of the optimal catalyst (5 %-S/N@BC) was conducted at C.A.C.T.I., University of Vigo (Vigo, Spain). Scanning Electron Microscopy with Energy Dispersive X-ray Spectroscopy (SEM-EDX) was performed using a JEOL JSM-6700F SEM equipped with an Oxford Inca Energy 300 X-ray EDS. XPS measurements utilized monochromatic Al-Kα radiation (1486.6 eV), collecting photoelectrons at a 90° angle relative to the sample surface. Measurements were taken in

Constant Analyzer Energy mode (CAE) with 100 eV pass energy for survey spectra and 20 eV pass energy for high-resolution spectra. Charge referencing was done by setting the lower binding energy C 1s photo peak at 284.80 eV (C1s hydrocarbon peak). Surface elemental composition was calculated using standard Scofield photoemission cross sections. X-ray diffraction patterns were obtained from powdered samples using a PANalytical X'Pert Pro diffractometer. This instrument was configured with a PW3050/60 goniometer, operating in a Theta/2Theta configuration, and utilized monochromatic CuK$\alpha_{1,2}$ radiation with a wavelength of 1.5406 Å, generated at 40 kV and 30 mA. The diffraction data were collected over a $2\theta$ angular range spanning from 5° to 70°, employing a continuous scanning mode at a rate of 0.0175° per second. Fourier Transform Infrared Spectroscopy (FTIR) was analyzed with a Thermo Fisher Scientific Nicolet 6700 fitted with an ATR accessory. FTIR spectra pre-processing was conducted using Orange data mining version 3.34 (Demšar et al., 2013). Rubber band baseline correction, truncation from 2715 to 1801.1 $cm^{-1}$, normalization with an extended multiplicative signal correction, and smoothing using the Savitzky-Golay algorithm (polynomial 2, window size 3, derivative order 0) were applied to all FTIR spectra. Raman spectra analyses were measured in a HR800UV (Horiba Jobin Yvon). The elemental composition of the obtained eco-electrodes was determined using a Fisons Carlo Erba EA1108 elemental analyzer. Finally, $N_2$ adsorption-desorption isotherms were made (3P Instruments Sync-200) for surface area determination following Brunauer-Emmett-Teller (BET) analysis. Thus, the porosity was calculated by applying the statistic thickness surface area model for carbon black (STSA) (Eq. (7)), commonly used for carbons, which evaluates the thickness of $N_2$ adsorbate as a function of relative pressure. From Eq. (7) curve, the volume and surface of micropores were obtained as intercept and slope, respectively [39].

$$t = 0.88\left(\frac{p}{p_0}\right)^2 + 6.45\left(\frac{p}{p_0}\right) + 2.98 \quad \text{(Eq.7)}$$

Barett-Joyner-Halendar (BJH) analysis of the $N_2$-desorption part was used for the calculation of the pore area, specific volume of pores and pore size distribution [40].

## 3. Results and discussion

### 3.1. Point of Zero Charge

The PZC is an essential parameter for assessing the surface acidity of the catalysts. Hence, it offers valuable insights into the acidic oxygen-containing functional groups present on the char surface. PZC is defined as the pH value at which the net charge of the catalyst surface is zero, being the positive and negative charges balanced. In accordance with this definition, a solution pH below the PZC causes a greater contribution of positive charges, while values above the PZC generate a predominant contribution of anions on the catalyst surface charge [41]. The obtained values of PZC for all samples are shown in Table 1. As illustrated, BC and S/N@BC samples exhibit a decreased surface acidity compared to the raw banana peel. This reduction is attributed to the dehydration and carbonization reactions occurring during pyrolysis, as well as the preservation of the inorganic fraction, which significantly contributes to the alkalinity of the BC [42]. Moreover, the PZC values of all S/N@BC are higher than BC, which can be interpreted as a reduction of the acidic oxygen-containing surface groups in the former, maybe due to an increase in N and S groups, and/or a more oxidized surface in the latter [43]. Consequently, the eco-electrocatalyst would be negatively charged at the working pH (14.09), favoring $H_2O$ disposition for promoting $O_2$ liberation (Fig. S1).

**Table 1**
PZC, intensity ratios from band G and band D from Raman spectra ($I_D/I_G$), charge transfer resistance (Rp) and system resistance (Rs) values for all tested materials.

| Sample | PZC ±SD | $I_D/I_G$ | Rs±SD | Rp±SD |
|---|---|---|---|---|
| Ni-Foam | – | – | 1.48 ± 0.05 | 2.62 ± 0.06 |
| Raw banana peel | 6.9 ± 0.1 | – | 0.69 ± 0.03 | 21.4 ± 0.78 |
| BC | 9.3 ± 0.4 | 0.95 | 1.32 ± 0.03 | 2.17 ± 0.03 |
| 2.5 %-S/N@BC | 10.9 ± 0.3 | 1.00 | 1.67 ± 0.05 | 1.84 ± 0.07 |
| 5 %-S/N@BC | 11.2 ± 0.2 | 1.12 | 1.47 ± 0.01 | 1.45 ± 0.04 |
| 10 %-S/N@BC | 11.3 ± 0.3 | 1.11 | 1.67 ± 0.04 | 1.92 ± 0.06 |

### 3.2. FTIR

BC and S/N@BC samples were examined using FTIR spectroscopy to analyze the surface functional groups within their carbon matrix, and the findings are illustrated in Fig. 3a. A reduction in oxygen-containing acidic groups can be observed in the S/N@BC electrodes, specifically with the clear reduction of –OH groups in the region of 3450 $cm^{-1}$ and C═O, associated with primary amides from banana peel proteins, and carboxylic groups. This is evident in the diminished bands on BC from the carbonyl C═O stretch near 1680 $cm^{-1}$ along with the band near 1616.2 $cm^{-1}$ involving the $NH_2$ bend and the band near 1405 $cm^{-1}$ involving the C–N stretch. The reduction in the carboxyl groups can be seen in the region around 1600 $cm^{-1}$ [44]. These results are consistent with the increase in PZC, indicating greater surface oxidation in BC compared to S/N@BC. A clear reduction in the C═C bonds corresponding to vinylidene alkene bending in the region of 875 $cm^{-1}$ can also be observed [45]. This provides clues about the interaction between these bonds and the N and S atoms of thiourea during the synthesis process. Identification of N-functional groups is influenced by bond energy and repulsive forces, further impacted by other atoms or groups. However, three distinctive bands appeared at 1512, 1548.6, and 1564.24 $cm^{-1}$ in the IR spectra of all S/N@BC samples, particularly prominent in the 5 %-S/N@BC. These bands are likely attributable to contributions from pyridinic and pyrrolic N structures [46]. There is also a significant increase in the region between 1240 and 1070 $cm^{-1}$, associated with quaternary or graphitic N, being the peak at 1121.1 $cm^{-1}$ associated with C–N stretching vibration [47,48]. Regarding the S-doping, distinct peaks at 1140 and 1192 $cm^{-1}$ indicate the presence of C═S stretching in thiocarbonyl groups. Additionally, the 1033 $cm^{-1}$ peak observed in all S/N@BC electrodes, highlighted on the 5 %-S/N@BC corresponds to S═O bending in sulfoxides [44,49]. In addition, bands appearing in the fingerprint region further substantiate the presence of symmetric and asymmetric stretching vibrations of S. For example, an increase at 608 $cm^{-1}$ confirmed the presence of C–S bonds [44]. Based on these results, it is conclusively demonstrated that the doping process successfully introduces N and S into the carbon matrix of the synthesized electrodes, particularly in the case of the 5 %-S/N@BC electrode.

### 3.3. RAMAN

Raman spectra of carbon-based catalysts characteristically exhibit two distinguishable bands (Fig. 3b): the G band at 1580 $cm^{-1}$, linked to $sp^2$ carbon that reflects the hybridization degree of the carbon material, and the D band at 1350 $cm^{-1}$, associated with $sp^3$ carbon atoms resulting from graphite crystal defects or disorder [50]. The ratio of the intensities of these bands ($I_D/I_G$) serves as an indicator of surface defects on the catalyst; the higher the $I_D/I_G$, the greater the number of defective sites [49]. The extent of defects in a carbon-based catalyst greatly impacts its performance, primarily due to the contribution of free π-electrons from the $sp^2$-hybridized carbon network [50].

In Fig. 3b the Raman shift for all the catalysts synthesized is displayed and in Table 1 the $I_D/I_G$ values are presented. The growth of defects and the small size of the $sp^2$ domains were verified by the ascending $I_D/I_G$ value of the S/N@BC samples, which was further augmented as the percentage of thiourea in the biochar synthesis increased until it slightly decreased on the 10 %-S/N@BC. Creating

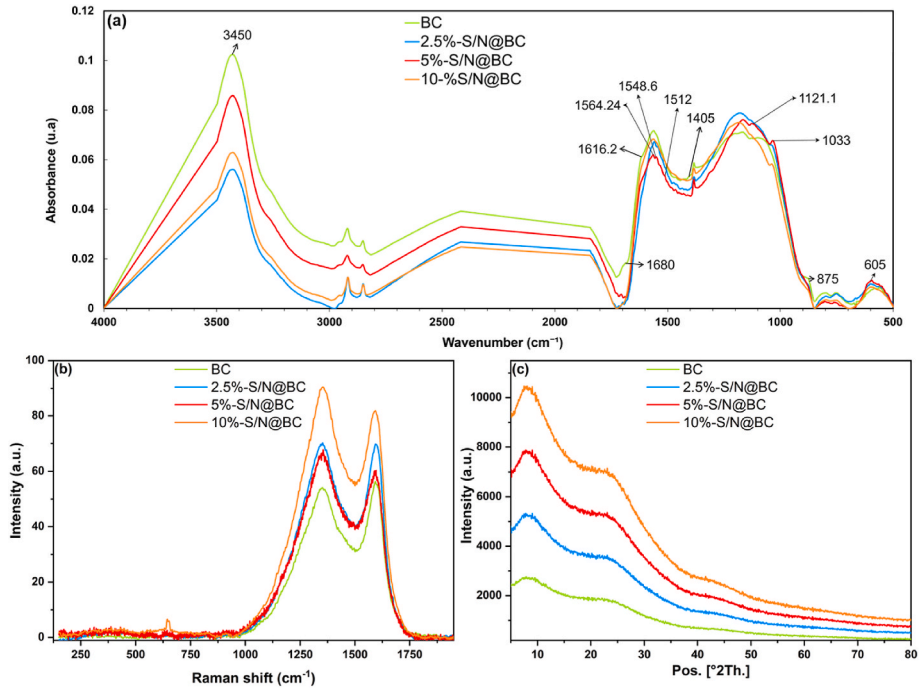


**Fig. 3.** FTIR (a) and Raman spectra (b), XRD patterns (c) for all synthesized catalysts.

these disordered carbon structures through N/S-doping is advantageous as it generates additional active sites and enhances electrical conductivity, thereby boosting electrochemical performance [51]. Structural defects present in the S/N@BC catalyst evidenced by Raman measurements, have been identified as active sites for the water splitting process [49]. Specifically, graphitic N and pyridinic N exhibit superior electro-catalytic activity compared to pyrrolic N, which is the main N form present in the S/N@BC as corroborated by FTIR data. Furthermore, the catalytic activity of doped S atoms is significantly enhanced in the synergistic presence of N atoms [49]. The eco-electrocatalyst that exhibited the greatest disorder and, therefore, had the highest number of defect sites was the 5 %-S/N@BC with an $I_D/I_G$ value of 1.12. These findings related to the increase in defects due to doping with heteroatoms have been supported by other authors, as reported by Xia et al. [25], who synthesized a S-self-doped biochar and observed an increase in defects ($I_D/I_G$ = 1.01) compared to the undoped sample ($I_D/I_G$ = 0.88). Similarly, Lian et al. [52] reported that a N-doped biochar derived from crop straws increased the $I_D/I_G$ value from 0.75 to 1.06. Consequently, banana peels proved to be a more suitable raw material for biochar synthesis (with a higher $I_D/I_G$ ratio) and the doping with thiourea provided up to $I_D/I_G$ = 1.12, which could be consistent with high catalytic activity.

### 3.4. XRD

Fig. 3c presents the XRD patterns obtained in 2$\theta$ ranging 10°–80° to study the crystallinity of the BC and S/N@BC catalysts. The absence of sharp diffraction peaks proves that there are no crystalline phases in the materials [30]. XRD analysis revealed a broad peak around a 2$\theta$ angle of 23° and another with less intensity at roughly 44°, both indicative of (0 0 2) and (1 0 0) reflection of a disordered/amorphous carbon phase [23]. The faint intensity of the (1 0 0) reflection indicates the carbon sample's low crystallinity, which aligns with the previous Raman analysis (section 3.3) [53]. Similar patterns were reported by Abdullah et al. [22] when characterizing banana peel derived biochar that was doped with urea and then used as OER-electrode. Consistent with the Raman results, slight differences were observed with the level of thiourea used in the synthesis, just as Sreńscek-Nazzal et al. [30] found no differences between banana peel-derived biochar and urea-doped banana peel-derived biochar.

### 3.5. SEM-EDS

The surface analysis of the synthesized materials was conducted using SEM-EDS (Fig. 4 and Fig. S2). The initial observation in Fig. 4 reveals a significant transformation from BC to S/N@BC materials. Although the synthesis temperature is not particularly high to promote the development of extensive porosity, the shift towards a more porous material with a uniform distribution of this porosity is evident on S/N@BC. This may be attributable to the addition of thiourea and the production of gases like ammonia during the synthesis process [54]. The porosity might enhance OER performance by promoting catalytic reactions due to the disordered morphology being intrinsically related to ECSA measurements [51]. In fact, for OER, defects in the carbon matrix led to facilitating the adsorption and desorption of OER intermediates [49]. However, the porosity developed in 10 %-S/N@BC material is lower than in the other S/N@BC, which could indicate a collapse in the pores due to an excess of doping [55]. EDS analyses are shown in Fig. S2. EDS analysis showed the doping is homogeneous throughout the BC surface, ensuring stable catalytic activity. It can be distinctly observed that the concentration of N and S on the surface of the samples increases as the percentage of thiourea used in the one-pot synthesis process is increased. These findings are consistent with those reported by other authors when performing co-doping in carbon-based materials as is the case of Li et al. [49] with N/S co-doped graphene as a defect-rich carbocatalyst for its usage on water splitting and Huo et al. [56] who used a N/S co-doped porous carbon obtained from sawdust for pollutants' adsorption.

To validate the effectiveness of the doping process, CHNS elemental analysis was conducted on all eco-catalysts synthesized in this study, with the results detailed in Table S1. The elemental analysis reveals significant compositional changes across banana peel-derived samples. Initially, the raw banana peel consists of 39.87 % C and 1.89 % N. However, after undergoing pyrolysis, the carbon content significantly rises to 72.77 %, while N increases slightly to 2.75 %. In contrast, H content decays from 5.67 % to 2.21 %, reflecting the loss of volatile

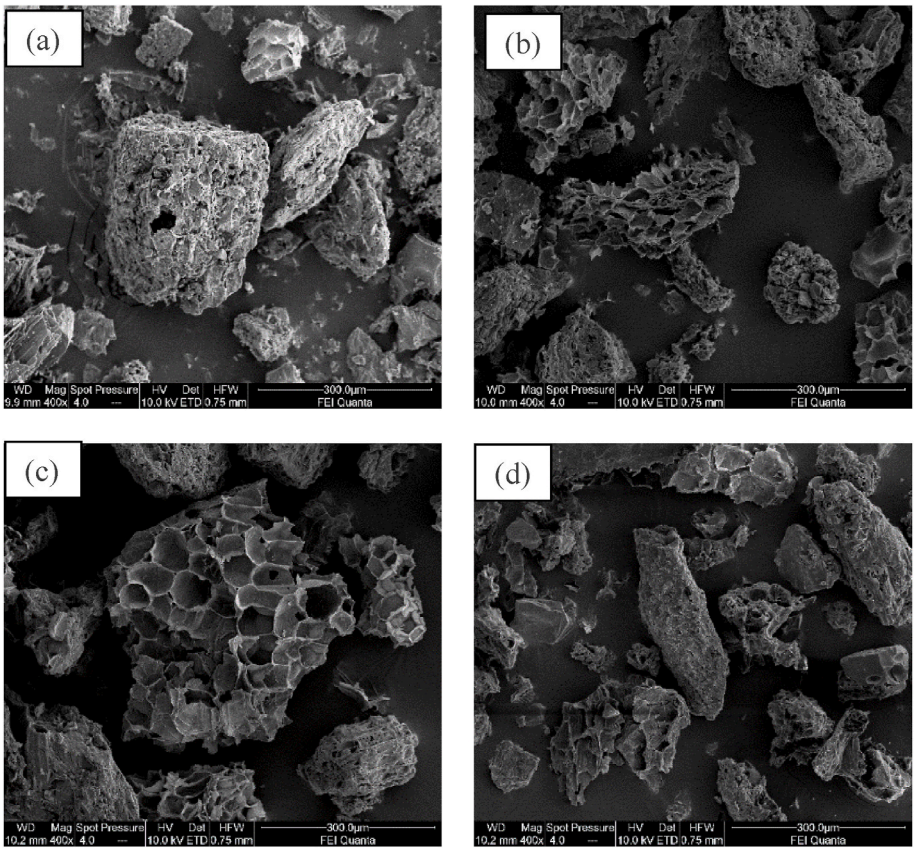


**Fig. 4.** SEM images of the different synthesized materials: (a) BC, (b) 2.5 %-S/N@BC, (c) 5 %-S/N@BC and (d) 10 %-S/N@BC.

components during carbonization [57]. Subsequent S/N@BC treatments demonstrate controlled heteroatom incorporation: N content progressively increases from 3.33 % (2.5 %-S/N@BC) to 6.39 % (10 %-S/N@BC), paralleled by S rising from 0.85 % (BC) to 2.36 % (10 %-S/N@BC). These trends indicate successful synthesis of N/S@BC carbon matrices. These results are consistent with the study by Sreńscek-Nazzal et al. [30], which reported a 5.8 % N content after doping banana peel with urea (1:1 mass ratio) at a lower temperature (700 °C). In fact, their study reported a decrease in N content with increasing temperature. Therefore, our findings are consistent, as we used a relatively lower doping temperature (550 °C compared to 700 °C), which helps preserve a higher N content.

### 3.6. BET

The $N_2$ adsorption-desorption analysis provided the data depicted on Table S2. As illustrated, biochar from banana peels exhibited negligible porosity whereas the addition of thiourea created new pores. This is in concordance with previous authors, which also noticed a BET increase after N [58,59] or S doping [60]. For instance, similar to this study, N incorporation in banana peels biochar through urea doping caused the increase on surface area after the synthesis at mild temperatures [30].

As seen in Fig. 5, the materials doped with 5 and 10 % thiourea exhibited mesoporosity [30]. 5 %-S/N@BC exhibited even a microporous structure, where the $N_2$ adsorbed increased at low relative pressures. This is apparent on the depicted micropore area measured (176.5 $m^2\ g^{-1}$). This multiplicity surface area due to N/S doping at appropriate dosages ensures the creation of ion transport channels which promote electrochemical activity [61]. Hence, mesopores presence reduces electrolyte diffusion resistance whereas macropores act as electrolyte transporters [61].

Specifically, the maximum porosity was obtained in 5 %-S/N@BC. This material exhibited an isotherm type IV, due to its high content of mesopores, showing a monolayer formation at low relative pressures and the condensation on the mesopores is noticeable on the hysteresis loop (Fig. 5a) [60]. This hysteresis loop is only present on the S/N doped

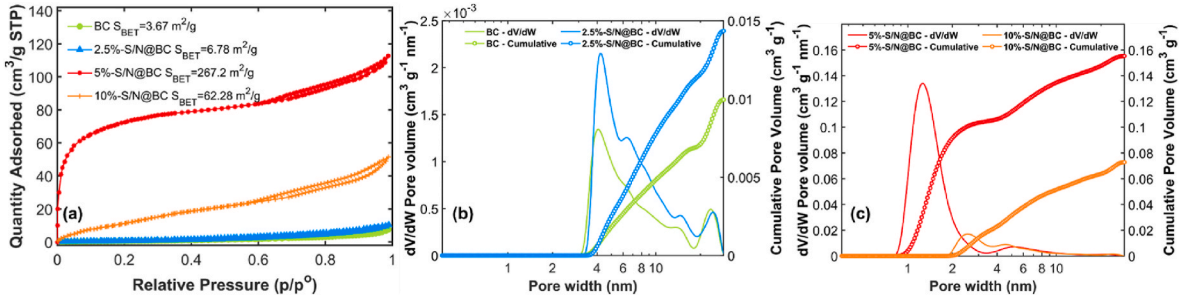


**Fig. 5.** $N_2$ Isotherms of the synthetised materials from banana peels (a), pore size distribution of BC and 2.5 %-S/N@BC (b), and pore size distribution of 5 %-S/N@BC and 10 %-S/N@BC (c).

biochars [59], demonstrating this treatment promotes mesopore and micropore generation. This isotherm type IV has been previously found for biochar-based materials due to biomass decomposition and gases generation [59,60].

The higher BET of 5 %-S/N@BC achieved when compared to the other materials synthesized is beneficial for the subsequent catalytic activity, as the active sites are more exposed [58]. Nevertheless, increasing the N/S doping to 10 %-S/N@BC caused a decrease on BET, due to the coverage of the BC structure with thiourea [55,62] as previously suggested by the EDS images (section 3.5).

As noticed on pore distribution plots (Fig. 5b,c), the pores range from 2 to 10 nm, linked to mesopores presence [31] which are dominant in all the samples but 5 %-S/N@BC. The more homogeneous pore size distribution of 5 %-S/N@BC (Fig. 5c), causes it to have a higher BET than the other synthetised catalysts [63]. Fortunately, 5 %-S/N@BC exhibited a higher pore volume than previous studies based on biochar [64,65]. However, the addition of more thiourea on 10 %-S/N@BC caused the pores to clog and reduce their size to mesopores [65]. On the case of BC and 2.5 %-S/N@BC (Fig. 5b) the insignificant pore amount is mainly distributed as mesopores. Thus, regarding 5 %-S/N@BC, its high content of micropores with a certain amount of mesopores and the big pore volume would favor the presence of electro-active sites [64] which may promote water splitting reactions.

### 3.7. Electrochemical measurements

#### 3.7.1. Cyclic voltammetry

The electrocatalytic behavior of the samples was measured by cyclic voltammetry (CV). When examining the CV in Fig. 6a (and Fig. S3) it became clear that the eco-electrocatalyst 5 %-S/N@BC exhibited superior OER performance compared to the other S/N@BC samples and Ni-Foam, as demonstrated by the higher current density (mA $cm^{-2}$) outputs achieved at the same applied overpotential (mV). Samples BC and 2.5 %-S/N@BC delivered similar electrocatalytic behavior, probably indicating that that level of S/N-doping was not sufficient for redistributing the charges in the carbon matrix. Likewise, 10 %-S/N@BC and Ni-Foam

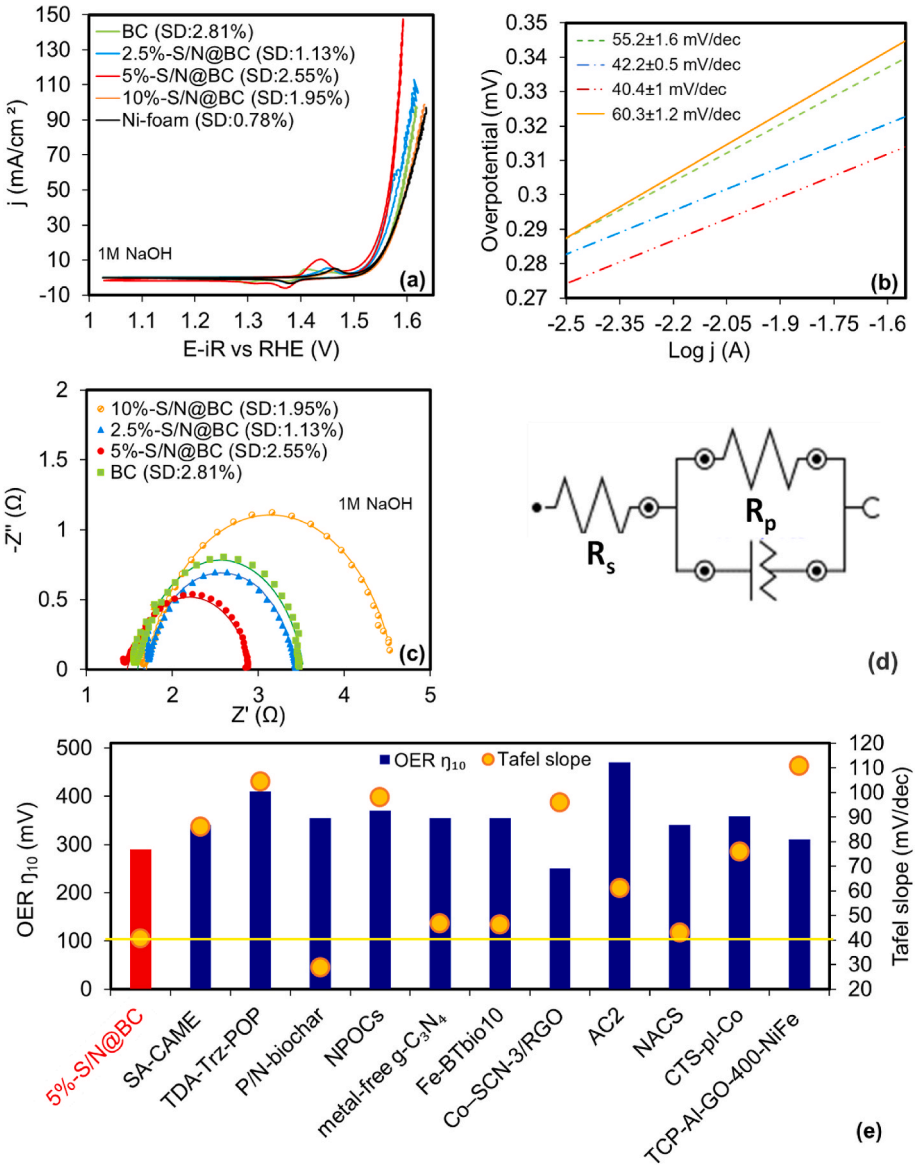


**Fig. 6.** Electrochemical characterization of all synthesized samples in 1 M NaOH: CVs (a), Tafel slope (BC in green, 2.5 %-S/N@BC in blue, 5 %-S/N@BC in red and 10 %-S/N@BC in orange) (b), Nyquist plot (c), Nyquist simulated circuit (d) and a performance comparison of the OER activity of 5 %-S/N@BC with other reported similar materials. See Table S4 for more details and references (e). SD is shown in brackets for each sample. (For interpretation of the references to colour in this figure legend, the reader is referred to the Web version of this article.)

presented similar results between them but worse than BC and 2.5 %-S/N@BC, which might indicate that a higher level of doping makes catalytic performance worse rather than better [26]. A drastic reduction in the overpotential values can be observed when introducing BC and S/N@BC onto bare Ni-Foam to reach specified current densities of 10, 50, and even 100 mA $cm^{-2}$, indicating good catalytic activity and an improvement in practical effectiveness. Particularly, the 5 %-S/N@BC sample showed remarkable performance, achieving 290 mV for *j* of 10 mA $cm^{-2}$ ($\eta_{10}$) and a Tafel slope value of 40.4 mV $dec^{-1}$. These experimental overpotential outputs are significantly low, even when compared to other commercial metallic catalysts such as $IrO_2$ (320 mV for *j* of 10 mA $cm^{-2}$) [66] or $RuO_2$ (350 mV for *j* of 10 mA $cm^{-2}$) [67]. Furthermore, the results surpass those reported by other authors using some types of carbon-based metal-free materials (Fig. 6e and Table S4); for instance, Xia et al. [25] reported an overpotential of 362 mV for 10 mA $cm^{-2}$ when testing a biochar from *Camellia japonica* [68]. Not only is the performance achieved by the S/N@BC materials significantly superior to other carbon-based metal-free materials, but even when compared to studies using carbonaceous materials doped with different metals, the results of this study still demonstrate a remarkable difference. For instance, Lofek et al. [24] reported overpotential values ranging from 358 to 372 mV for 10 mA $cm^{-2}$ using various cobalt-doped biomasses. Similarly, the performance of 5 %-S/N@BC is very similar to that reported by other authors using a Ni–Fe electrode supported by N-rich graphene oxide derived from algae, needing an overpotential of 310 mV for 10 mA $cm^{-2}$ [68]. Additionally, sample 5 %-S/N@BC, which peaked at 147.7 mA $cm^{-2}$ at an overpotential of 336 mV, also presented the highest anodic and cathodic peaks among the rest of the samples at 1.43 and 1.37 V *vs.* RHE, respectively. This pre-oxidation peak is intrinsically related to the $O_2$ evolution at the anode due to the adsorbed hydroxyl groups [6], providing further evidence of the sample's impressive performance as an electrocatalyst for OER. In order to elucidate the particular influence of S in the doping process, a comparative experiment was carried out. In this experiment, urea-doped BC (5 %-N@BC) was utilized as a substitute for thiourea. As demonstrated in Fig. S4, the electrochemical performance was reduced significantly in the absence of S, proving a critical contribution of S to the doping mechanism. This finding is supported by recent studies regarding the critical contribution of S to the doping mechanism and electrocatalytic performance of the materials [69]. It has been reported according to the Density Functional Theory (DFT), that the process of co-doping with N and S modifies the electronic and spin structures of the material [69]. This enhanced mechanism is rooted in two fundamental factors. First, the higher electronegativity of N leads to charge polarization through electron-withdrawing effects [70]. Second, S larger atomic radius when compared to N generates structural defects and asymmetric spin density, with its p-orbital electrons extending π-systems to improve oxygen interactions [71]. Consequently, N/S-co-doping disrupts $sp^2$ structures in a synergistic manner, enabling charge delocalization that optimizes conductivity, as well as increasing the population of catalytically active carbon sites and reducing charge transfer resistance [70].

### 3.7.2. Tafel slope

Tafel slopes of all the samples analyzed are presented in Fig. 6b (and Fig. S3). The performance of the bare Ni-Foam electrode is included for a better comparison with the synthesized BC and S/N@BC samples. A lower Tafel slope indicates quicker reaction kinetics and greater activity of the electrocatalyst [72]. Clearly, both the overpotential and Tafel slope show the one-pot S/N co-doping causes a significant OER performance, being 5 % the optimal doping. This could be explained considering that N-doping introduces active functional groups that enhance OER and reduce carbon corrosion, improving selectivity for $O_2$ reduction over CO or $CO_2$ [73]. On the other side, S-doping increases the carbon atom's charge density, facilitating charge transfer and boosting catalytic activity [25]. The substitution of an N atom with an S atom is known to result in the nearby carbon atom losing fewer electrons to the surrounding carbon network. Considering electronegativity values (N > S ≈ C), the doped site effectively donates electrons to electronegative oxygen species, strengthening carbon-oxygen interactions. However, excessive S-doping can lead to suboptimal stabilization, hindering OER [26] as revealed by the results obtained for the sample 10 %-S/N@BC. The results obtained by 5 %-S/N@BC are superior to those reported for $IrO_2$ with a Tafel slope of 76 mV $dec^{-1}$ [66] or $RuO_2$ with a Tafel slope 59 mV $dec^{-1}$ [67]. Additionally, this value surpasses all Tafel slopes reported by Li et al. [49], when doping graphene with different levels of N and S as defect-rich carbocatalyst for water splitting. Moreover, these results also surpass the performance of the ones reported by Jiang et al. [51] who studied carbon-based electrodes varying the doping heteroatom (S/N/P). Another noteworthy example is provided by the Tafel slope values reported in some studies that dope biomass with metals, which also obtained higher values than those obtained in this study, as seen in the case of cobalt-doped biomass [24] and Ni/Fe-doped biomass [68]. This highlights the highly competitive performance and kinetics rate of the metal-free 5 %-S/N@BC on OER.

### 3.7.3. Electrochemical impedance spectroscopy-Nyquist plot

The results derived from the EIS test can be seen in Fig. 6c, which interpretation is straightforward: the smaller semicircular radius at high frequency Z′, the lower charge transfer resistance and quicker electron transfer [6]. The direct implication is that the OER reaction would be favored in those cases. In the Nyquist plot, it can be observed that the smallest arc is exhibited by the 5 %-S/N@BC sample, which correlates with lower Tafel values and enhanced CV performance, reflecting elevated electrocatalytic activity. Conversely, the largest arc, indicating the lowest performance, corresponds to the 10 %-S/N@BC and Ni-Foam electrodes. The intermediate values between these two extremes are observed in samples 2.5 %-S/N@BC and BC. When comparing these EIS data with those reported by other authors, a similarity can be observed between the study performed by Li et al. [74] and their Nyquist plot obtained for their optimal sample, $Co_3O_4$/BMC-400, and the 5 %-S/N@BC sample of this study. This is a promising result, as our metal-free S/N doped BC exhibited electron transfer capacity values comparable to those of mesoporous carbon-modified $CO_3O_4$ quantum dots doped with S/N.

Key parameters extracted from the EIS simulated circuit (Fig. 6d and Table 1) are the system resistance (Rs) and charge transfer resistance (Rp) which measure the system resistivity and polarization resistance respectively [75]. On one side, Rs, series resistance, is affected by the setup, electrolyte, catalyst layer, and the ohmic resistance of the electrolyte between the reference and the working electrode [36]. All tested electrodes exhibited comparable Rs, ranging from 1.3 to 1.69 W (see Table 1), indicating a high degree of consistency in the experimental setup and conditions [76]. On the other side, Rp represents the resistance to charge transfer at the electrode-electrolyte interface and can be associated with various physical properties such as kinetics of electrochemical reactions, mass transfer barriers and diffusion mechanisms. Fundamentally, Rp provides information about the efficiency and output of electrochemical reactions within the system. It is defined as the resistance of the electrolyte to oxidation when an external potential is applied. Additionally, Rp values are inversely proportional to the rate of electrochemical oxidation [77]. As seen in Table 1, bare Ni-Foam delivered the highest Rp value, linked to an inferior electron transfer capacity, while all S/N@BC catalysts significantly reduced that value, specially the 5 %-S/N@BC samples that yielded the lowest Rp scores, suggesting their greater capacity for electrochemical oxidation in the presence of oxygen, hydrogen or hydroxide [36]. The Rp values obtained are lower than those reported for $Co_3O_4$ quantum dots [74]. However, when comparing these results with those reported by Xia et al. [25] using a carbon-based sulfur self-doped multifunctional biochar catalyst, we observe that the values obtained in this study are slightly higher, suggesting that the electron transfer capacity is lower in our

case. Nonetheless, these small variations could also be attributed to the different setups used in each study, as the electrodes and electrolytes vary, potentially affecting the impedance values.

All these data are consistent with those found so far both in the CV and Tafel, reflecting again that the 5 %-S/N-doping applied in this study is successful and delivers outstanding results in terms of OER performance. A potential reason for the improved results could be that the inherent nature of BC derived from banana peel gives rise to a defective structure. This unique structural characteristic provides a favorable framework for the incorporation of N and S active sites during the doping process. These active sites stabilize and strengthen the interaction between the critical intermediates and the catalyst, thereby further amplifying its proactive influence on OER catalytic activity [10].

### 3.7.4. Electrochemical Active Surface Area

Electrochemical Active Surface Area (ECSA) serves as a crucial metric for assessing the effective working area available for catalysis, as catalysts with high ECSA facilitate water splitting processes [78]. To determine ECSA, multiple CV curves were recorded at varying scan rates (see Fig. S5 for details), where the resulting current response was attributed solely to capacitive behavior (non-Faradaic process). From these CV data, a plot of current density (mA $cm^{-2}$) against scan rate (mV $s^{-1}$) (Fig. 7a) was used to estimate the geometric double-layer capacitance (CDL). Since CDL provides a direct measure of an electrocatalyst's ECSA, a higher CDL indicates greater ECSA and, consequently, superior electrocatalytic performance [78], being 3.4 mF $cm^{-2}$ the value obtained for 5 %-S/N@BC. Hence, a greater ECSA leads to increased absorption of water molecules and intermediates on the catalytic material surface, thereby offering more electrochemically active sites. This enhancement is advantageous for improving both the rates of HER and OER [51]. The trend of electrodes doped with S/N is clearly observable (Fig. 7b), with ECSA values notably increasing and reaching a significant maximum of 78.5 $cm^2$ for the 5 %-S/N@BC eco-electrocatalyst. However, the ECSA values decrease for the 10 %-S/N@BC electrode, likely due to the structural collapse and reduced pore size resulting from excessive S/N-doping within the BC matrix [55] as corroborated by EDS images and BET analysis. This value is consistent with the SEM superficial analyses and with the exceptional results achieved by 5 %-S/N@BC electrode in OER measurements. Comparing these values with those of other metal-based catalysts, we observe that our catalyst provides competitive results. For instance, Patel et al. [79] studied metal-organic framework-derived core-shell nanoparticles and reported an ECSA value of 3.7 $cm^2$. Furthermore, the values for 5 %-S/N CDL and ECSA exceeded those obtained by Ghosh et al. [80] with a metal-free thiadiazolate-based N and S-rich porous organic polymer, reporting a CDL value of 1.27 mF $cm^{-2}$ and a corresponding ECSA of 3.8 $cm^2$. Conversely, when compared with other carbon-based electrodes with higher porosity due to their nature or higher synthesis temperature reported in the literature, our results are slightly lower. For example, Ma et al. [32] reported a CDL value of 6.1 mF $cm^{-2}$ for an N/P-doped biochar electrode synthesized at 800 °C from agricultural residues. Similarly, Zhang et al. [33] reported a CDL value of 6.8 mF $cm^{-2}$ for an N/P/O-doped 3D porous nanostructure. Consequently, the hereby attained equilibrated ECSA values may favor the superior OER activity found with 5 %-S/N@BC.

## 3.8. Additional evaluation of 5 %-S/N@BC electrode

Given that 5 %-S/N@BC emerged as the most effective option among the four electroactive substances evaluated, this section focused on conducting a more in-depth examination of this catalyst.

### 3.8.1. Effect of catalysts dose and pH

The optimal OER properties were observed with a catalyst loading of 1 mg $cm^{-2}$. It can be easily interpreted from Fig. 8a that increasing the 5 %-S/N@BC content on the Ni-Foam support beyond this level had a negative effect while lower loadings resulted in insufficient performance. Comparable results were reported by Torres-Pinto et al. [34], who optimized the catalyst loading on the electrode. They found that, under identical experimental conditions and setup to those used in our work, they also identified the same optimal loading. On the other hand, the authors using a biochar derived from tea extract-doped with Fe [81] found an optimal catalyst loading of 0.25 mg $cm^{-2}$. They noted that at higher loadings, nanoparticle agglomeration could block active surface sites, reducing the effective surface area, likely due to excess Fe occupying available sites. Therefore, it is possible that removing metals from the electrodes necessitates a higher catalyst loading to maintain performance. Thus, finding the precise balance in catalyst loading is crucial to achieving the best possible electrocatalytic activity, as excessive catalyst amounts can obstruct or block the accessibility of active sites reducing efficiency, while too little can impede effective charge transfer on the electrode surface, both of which negatively impact overall electrode performance [82].

Although many doped carbon materials exhibit remarkable electrocatalytic activity individually for OER or HER, few can perform well simultaneously due to instability or inactivity in unfavorable pH environments [83]. Consequently, considering the robust performance of the 5 %-S/N@BC in alkaline OER, we explored its efficacy over a range of pH environments (Fig. 8b). As expected, the neutral and acidic OER demonstrated subpar performance. This can be attributed to the fact that under acidic conditions, an energy input of 1.23 V is required for electrochemical water splitting compared with 0.4 V in alkali conditions [84]. However, the slow reaction rates of HER and OER necessitate significant overpotentials to achieve substantial current density, thereby reducing energy conversion efficiency. Consequently, the actual voltage required for water splitting exceeds 1.23 V by a considerable margin [85]. Thus, while the 5 %-S/N@BC eco-electrocatalyst required an overpotential of 993 mV for achieving $j$ of 3 mA $cm^{-2}$ under neutral

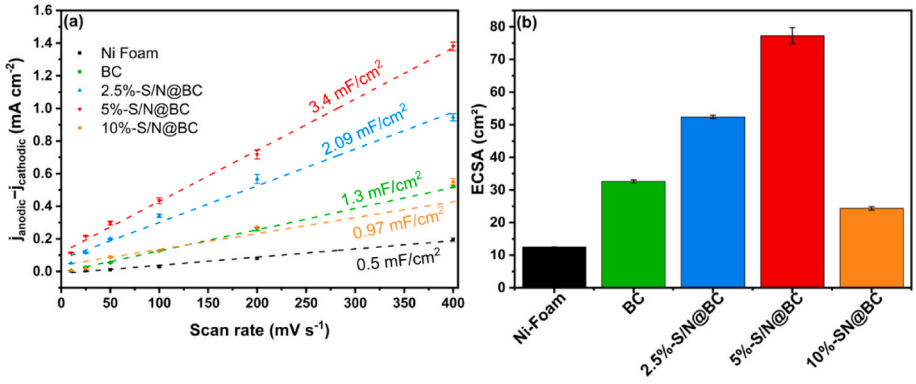


**Fig. 7.** Data obtained from ECSA measurements: CDL (a) and ECSA values (b).

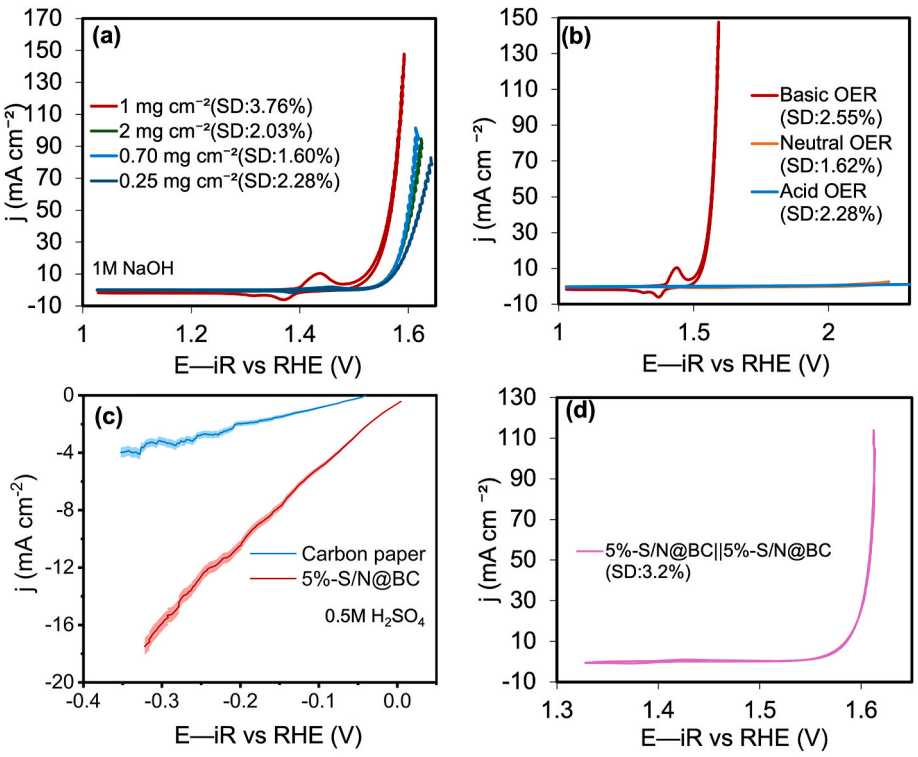


**Fig. 8.** Analysis of OER performance with the 5 %-S/N@BC electrode as influenced by varying catalyst mass loading (a), OER CVs performances at different pH (b), HER performance of 5 %-S/N@BC and carbon paper in acid media (c), and polarization curves of 5 %-S/N@BC for overall water splitting in alkaline conditions (d). SD is shown in brackets for OER CVs and as a shadow in HER.

conditions and an only 584 mV for *j* of 7 mA $cm^{-2}$ under acidic conditions, its performance still fell short of that achieved under alkaline conditions. Similar results were reported by Dominguez-Alonso et al. [81] when using a tea extract biochar loaded with 10 %wt. Fe. However, Torres-Pinto et al. [34] using g-$C_3N_4$ achieved excellent electrocatalytic performance in acidic and even neutral media, attributing it most likely to the amphoteric nature of $C_3N_4$. Therefore, improving this aspect of the catalyst in the present study should be considered. Nevertheless, current scale-up $H_2$ generation is carried out at alkaline pH as is the case of Alkaline Water Electrolysis cells (AWE) and Anion Exchange Membranes (AEM) [86].

### 3.8.2. *Hydrogen evolution reaction and overall water splitting*

In the case of acidic HER (Fig. 8c), achieving 10 mA $cm^{-2}$ required an overpotential of 200 mV, demonstrating some HER catalytic activity when compared to the near 400 mV needed for carbon paper alone to achieve a maximum of 4 mA $cm^{-2}$. This result is promising, as the performance exceeds previous studies on non-metal catalysts. For instance, to reach 10 mA $cm^{-2}$, Li et al. [49] required 310 mV for their N and S co-doped graphene as defect-rich carbocatalysts in acid media and García-Dalí et al. [87] reported a value of 270 mV for a phosphorus-doped carbon-based electrocatalyst. However, although very close to our value, Xia et al. [25] reported an overpotential of 154 mV at 10 mA $cm^{-2}$ for their S self-doped carbon nanospheres. Similarly, Atchudan et al. [23] achieved 10 mA $cm^{-2}$ at an overpotential of 150 mV using their $MoS_2$@BPPC/CC catalyst, which was derived from banana peel-derived but doped with the metal molybdenum. Consequently, further studies would be focused on additional 5 %-S/N@BC modifications in order to enhance this promising HER performance.

As previously noted, current large-scale $H_2$ production is primarily conducted using AWE or AEM cells, both operating in alkaline media [88]. In light of this and motivated by the remarkable alkaline OER performance exhibited by 5 %-S/N@BC, we further investigated its bifunctional potential for overall water splitting (OWS) in alkaline conditions to gain deeper insight into its catalytic efficiency. In this system, 5 %-S/N@BC was uniformly deposited onto carbon paper for use as the cathode and onto Ni foam for use as the anode. As it can be seen in Figs. 8d and 5 %-S/N@BC could also serve as a bifunctional electrocatalysts for driving alkaline OWS, with a notably low cell voltage of 1.58 V required for reaching 10 mA $cm^{-2}$. This means that the system proposed here demonstrates clear advantages over most previously reported electrocatalysts, including those not based on biomass [89]. The obtained Tafel slope of 59.2 mV $dec^{-1}$ is still within the range of values reported by other studies using carbon-based catalysts only in OER performance (Table S4). Therefore, as evidenced by Fig. 8d and Table S4, these results are markedly superior than those reported in other studies employing biomass-based electrodes, such as those by Xia et al. [25]. Finally, the energy efficiency of the cell during OWS was calculated (Fig. S7a), being higher than 75 % even at the highest potential, meaning that the cell operates with a remarkably low energy loss and high conversion efficiency. As a comparison, Xia et al. [25] reported a voltage of 1.76 V in their electrolytic cell during OWS to reach a current density of 10 mA $cm^{-2}$ using a S self-doped biochar, translating to an energy efficiency of 70 %. Likewise, Zhang et al. [33] used a N/P/O@doped porous carbon, registering a voltage of 1.9 V under comparable conditions, which yield an energy efficiency of 65 %.

### 3.8.3. *Stability tests*

Chronopotentiometry measurements were conducted at current densities of 10, 50, and 100 mA $cm^{-2}$ to assess the electrochemical stability of the 5 %-S/N@BC and $IrO_2$ catalysts and the results are presented in Fig. 9a–c. The overpotential stability of the 5 %-S/N@BC eco-electrocatalyst remained remarkably consistent, exhibiting an increase of less than 2 %, 5.90 % and 7.96 % from the initial overpotential over a continuous 30-h measurement period at 10, 50 and 100 mA $cm^{-2}$ respectively (Fig. 9a). These results are comparable to those reported by other researchers who synthesized various types of carbon-based electrodes, which have been reported to maintain stability for periods

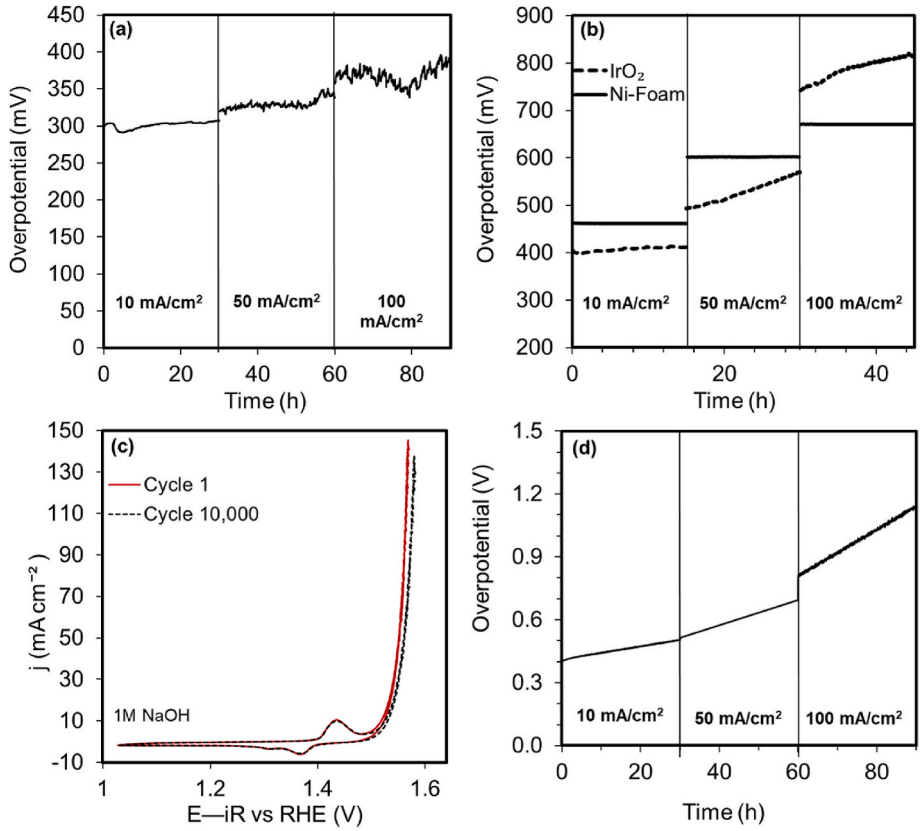


**Fig. 9.** Stability evaluation of 5 %-S/N@BC in alkaline medium: Chronopotentiometry analysis for 5 %-S/N@BC (a), and Ni-Foam and $TiO_2$ (b), ADT (c), and OWS stability (d).

ranging from 15 [34] to 50 h [51]. In contrast, $IrO_2$ (Fig. 9b) displayed great stable activity at 10 mA $cm^{-2}$ during 15h (400 mV); however, when applying higher current densities, the overpotential augmented considerably and steadily over the 15-h period, skyrocketing to values of 800 mV at 100 mA $cm^{-2}$ applied. Furthermore, chronopotentiometry analysis of Ni-Foam alone (Fig. 9b) revealed high overpotentials but demonstrated robust endurance to applied current intensities, highlighting its resilience as an effective support for carbon-based electrodes. The durability of materials is a critical factor in catalyst selection due to its direct impact on the effectiveness of the OER and overall process cost [7]. Thus, to further assess the stability throughout the entire OER potential range, ADT was conducted (Fig. 9c). These findings emphasize the superior electrochemical stability of the 5 %-S/N@BC eco-electrocatalyst, particularly when compared with the benchmark catalyst, highlighting the potential of this metal-free catalyst to enhance the OER.

The stability of the catalyst during alkaline OWS was also examined. The overpotentials obtained at three different current densities are shown in Fig. 9d. As expected, the overpotentials for OWS are higher than those observed in the original setup for OER at each applied current density (10, 50, and 100 mA $cm^{-2}$). For each 30-h period, a substantial increase can be observed, indicating that the stability is lower than in the OER study. Specifically, there is a 26 % increase at the end of the 10 mA $cm^{-2}$ period, a 37.7 % increase after the 30 h at 50 mA $cm^{-2}$, and a 40.9 % increase after applying 100 mA $cm^{-2}$. These results indicate that the catalyst undergoes greater degradation over time during OWS, and that at current densities closer to those used in commercial devices, the stability would not be optimal. All of this is related to the limited HER performance of the catalyst; however, numerous studies have considered the use of different cathode and anode materials [90,91]. In fact, $IrO_2$ and Pt/C are commonly used as benchmark catalysts for the OER and HER, respectively [6,7]. The average energy efficiency of the cell over the 30-h test at each current density was calculated (Fig. S7b). At the end of the 10 mA $cm^{-2}$ period, the average efficiency remains above 70 % while after the 50 mA $cm^{-2}$ interval, the efficiency decreased to 67.23 %. Finally, at the end of the 100 mA $cm^{-2}$ period, the efficiency was recorded at 55.5 %. These results indicate a clear trend of decreasing energy efficiency with increasing current density, highlighting the impact of operational conditions on the cell's long-term performance. Among the reasons for this high operational impact are that working at higher intensities reduces Faradaic efficiency due to the promotion of bubbles generation [92], the appearance of side reactions [93] and mass transfer limitations [94]. Nevertheless, some previous studies have shown lower energy efficiencies when evaluating OWS [25,33].

SEM images were taken to assess the morphological stability of the catalyst after the OWS stability test. In these images (Fig. S8), the same structures observed in the pristine material prior to use are still present at the end of the stability test, indicating that no substantial changes occurred. This, together with the stability data, suggests that the material is structurally robust enough to effectively withstand long periods of use in industrially relevant scenarios.

### 3.8.4. *X-ray Photoelectron Spectroscopy*

The content, types, and states of the surface constituent elements, particularly heteroatom species, in the prepared 5 %-S/N@BC eco-electrocatalyst were analyzed both before and after its long-term use through X-ray Photoelectron Spectroscopy (XPS) measurements. Results are presented on Fig. 10, the deconvoluted peaks in Table S3 and the survey spectrum in Fig. S6. Starting with the analysis of the pristine sample, Fig. 10a–c presents the fine spectra of C 1s, N 1s, and S 2p, respectively, for the 5 %-S/N@BC material before use, while Fig. 10d–f depicts the same spectra after 90 h of OER chronoamperometry testing. Fig. 10a reveals the presence of C–C and C═C (284.8 eV), together

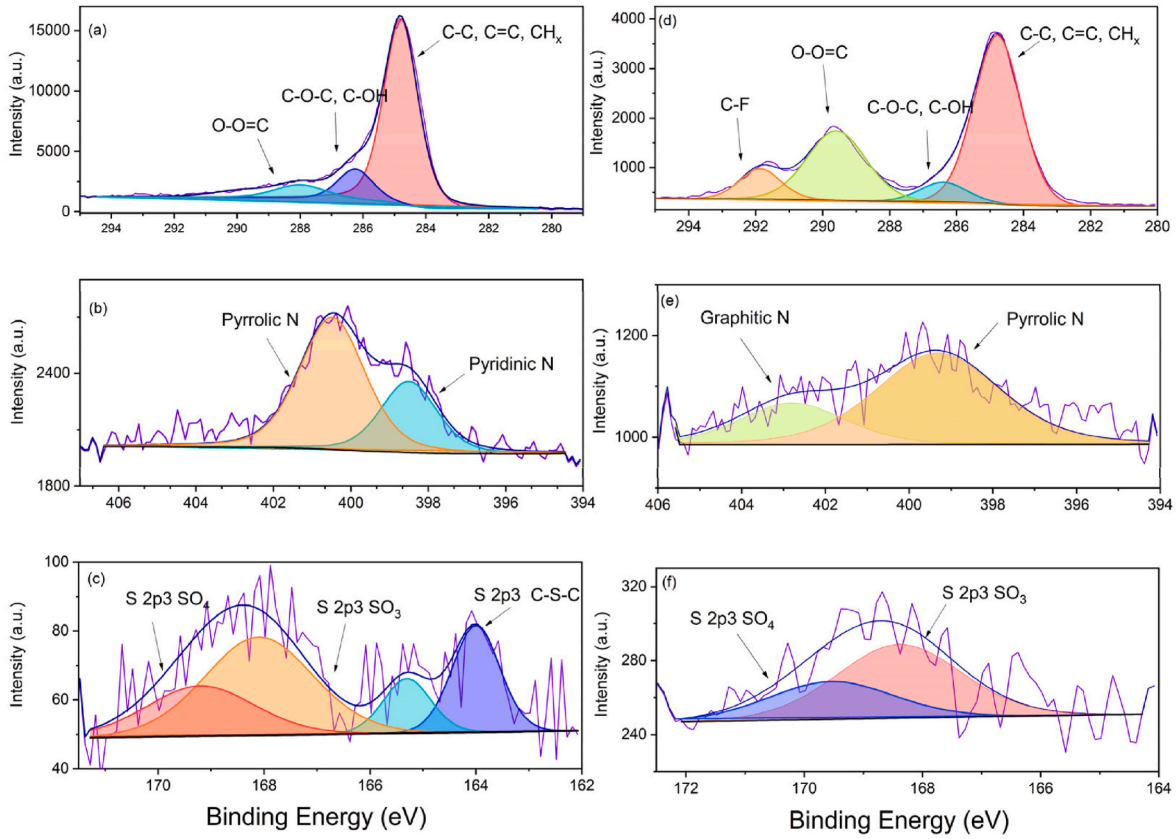


**Fig. 10.** 5 %-S/N@BC XPS deconvolution spectra before use for: C1s (a), N1s (b), S2p (c); and after use for: C1s (d), N1s (e), S2p (f).

accounting for 75 % At. It also shows more oxidized species such as C–O–C, C–OH (286.25 eV), and C═O–O (288.5 eV) [95], present at 18.25 % At. and 12.66 % At., respectively. The C–S and C–N bonds are somewhat overlapped by the peaks corresponding to C–O, given their similar energy levels and significantly lower abundance. Regarding N content, 31.6 % At. is identified as pyridinic N (398.5 eV) and 68.4 % At. as pyrrolic N (400.49 eV) [51] (Fig. 9b). This is significant as pyridinic nitrogen enhances notably the surface wettability of the electrocatalyst, promoting better electrolyte diffusion within the material. Additionally, pyridinic N elevates the electron density and boosts the electrocatalytic activity [96]. For S (Fig. 10c), surface analysis indicates that 7.12 % At. is present as thiophene C–S–C (163.7 eV) and 65.37 % At. as $SO_3/SO_4$ (168.1 and 169.2 eV) [27]. It has been suggested that the incorporation of thiophene S enhances catalytic kinetics by promoting the adsorption of intermediates, thereby boosting the overall electrocatalytic performance [51]. These results are consistent with, and thus validate, the findings from FTIR analyses. Turning to the results obtained after using the 5 %-S/N@BC, the C1s deconvolution (Fig. 10d) shows a clear shift from cyclic carbon towards oxidized forms, with C–O–C and C–OH decreasing to 6.36 % At. and C═O–O increasing to 28.8 % At., fact which is consistent with the application of the OER. The C1s peak in Fig. 10d that appears after use at 291.7 eV arises from $–CF_2$- group. Its presence in the sample is attributed to the binder used in this study, Nafion® [97] present due to the 5 %-S/N@BC extraction process based on EtOH extraction with ultrasonic cavitation from the Ni-Foam support. Regarding the N1s spectrum (Fig. 10e) after 5 %-S/N@BC use, significant changes were observed in the content of pyridinic N, pyrrolic N, and graphitic N. This time, it can be deconvoluted into two peaks: pyrrolic N at 398.5 eV which increased to 71.8 % At. after use, and a new peak of graphitic N, emerging at 402.790 eV with 28.2 % At. The disappearance of pyridinic N indicates that this species is the main active site in the OER process, and the maintenance of efficiency throughout the cycles can be attributed to the emergence of graphitic N, which has also demonstrated great electrocatalytic activity [49]. Finally, S2p presented only one peak at 168.39 eV indicating that all S was oxidized to $SO_3/SO_4$ (Fig. 10f) in the electrode. Hence, thiophene was confirmed to be a crucial active site in the OER process. These findings align with those reported by Jing et al. [51] on doping carbon-based electrodes with various heteroatoms (S, N, and P), as well as with the work of Li et al. [49], who achieved a defect-rich electrode for electrochemical water splitting by doping graphene with S and N.

The XPS spectra for S2p and N1s (Fig. 10c, d, 10f) showed lower signal-to-noise ratios than expected, likely due to XPS's surface sensitivity (~5–10 nm depth) and the catalyst's local heterogeneity [95]. Despite this, the spectra still offer valuable surface composition insights. Bulk CHNS analysis (Table S1) confirms successful N and S incorporation (e.g., 4.47 % N, 1.29 % S in 5 %-S/N@BC), highlighting the need for multimodal characterization to bridge surface and bulk discrepancies in such heterogeneous materials.

## 4. Conclusions

This study has demonstrated the feasibility of producing an efficient and functional eco-electrocatalyst for water splitting reactions entirely derived from agro-industrial waste. This approach addresses the dual challenges of excess waste and the need for renewable energy resources to support the growing global population. Thus, for the first time, banana peels were doped with thiourea in a one-pot pyrolysis synthesis for its usage on the challenging OER. The optimal eco-electrocatalyst obtained in this study, the 5 %-S/N@BC, has demonstrated highly competitive performance when compared to other more complex metal-free catalysts or even carbon-based catalyst doped with metals, defeating even benchmark $IrO_2$. Besides, this catalyst exhibited excellent stability over prolonged testing periods. Furthermore, it has been clearly demonstrated that one-pot S/N co-doping is a green and effective technique for reducing electrode overpotentials and, thus, increasing

overall water splitting efficiency. The exceptional performance obtained (290 mV for $j$ of 10 mA $cm^{-2}$, Tafel slope of 42.2 mV $dec^{-1}$) is highly competitive, not only among carbon-based electrodes but also in comparison with those containing a significant proportion of metals. The stability exceeding 90h without significant loss of electroactivity suggests that this catalyst could be considered even for industrially relevant applications. Despite the strong results, there is still room for improvement, particularly in acidic performance. Enhancing this aspect could lead to the development of a dual-function electrode suitable for both OER and HER. Indeed, overall water splitting was essayed and only 1.58 V were required for obtaining 10 mA $cm^{-2}$. The synthesis and successful use of 5 %-S/N@BC for the first time opens a path for large-scale applications considering the use of an environmentally friendly compound like thiourea and the single step syntheses process. This investigation sets the stage for advancing water splitting processes through cost-effective methods and minimizing environmental and economic impacts. The encouraging findings underscore the need for additional research to fully harness and refine the potential of this eco-electrocatalyst.

## CRediT authorship contribution statement

**Silvia Escudero-Curiel:** Writing – original draft, Validation, Investigation, Formal analysis, Data curation, Conceptualization. **Aida M. Díez:** Writing – review & editing, Visualization, Supervision, Project administration, Methodology, Investigation, Formal analysis, Conceptualization. **Marta Pazos:** Writing – review & editing, Supervision, Resources, Project administration, Funding acquisition. **Ángeles Sanromán:** Writing – review & editing, Supervision, Resources, Project administration, Funding acquisition.

## Data availability statement

The data that support the findings of this study are also available in the supplementary material of this article.

## Funding

This work has been funded by Project H2-ZeroWaste from AXA Research Fund, projects CINTECX-CHALLENGE 2023 and 2024 and MCIN/AEI/10.13039/501100011033 Project PID2020-113667 GB-I00. The researcher Aida M. Díez is grateful for the financial support RYC2023-044934-I funded by MICIU/AEI/10.13039/501100011033 and by FSE+. The researcher Silvia Escudero-Curiel is grateful to Xunta de Galicia for the financial support obtained (ED481B-109). Funding for open access charge: Universidade de Vigo/CISUG.

## Declaration of competing interest

The authors declare that they have no known competing financial interests or personal relationships that could have appeared to influence the work reported in this paper.

## Appendix A. Supplementary data

Supplementary data to this article can be found online at https://doi.org/10.1016/j.ijhydene.2025.150728.

## References

[1] van Hulst N. The clean hydrogen future has already begun. IEA Commentaries; 2019.
[2] Hermesmann M, Müller TE. Green, Turquoise, blue, or grey? Environmentally friendly hydrogen production in transforming energy systems. Prog Energy Combust Sci 2022;90:100996. https://doi.org/10.1016/J.PECS.2022.100996.
[3] Mehmeti A, Angelis-Dimakis A, Arampatzis G, McPhail SJ, Ulgiati S. Life cycle assessment and water footprint of hydrogen production methods: from conventional to emerging technologies. Environments 2018;5:24. https://doi.org/10.3390/ENVIRONMENTS5020024. 2018;5:24.
[4] Zhang L, Xiao J, Wang H, Shao M. Carbon-based electrocatalysts for hydrogen and oxygen evolution reactions. ACS Catal 2017;7:7855–65. https://doi.org/10.1021/ACSCATAL.7B02718/ASSET/IMAGES/LARGE/CS-2017-02718P_0012.JPEG.
[5] Liang Q, Brocks G, Bieberle-Hütter A. Oxygen evolution reaction (OER) mechanism under alkaline and acidic conditions. J Phys: Energy 2021;3:026001. https://doi.org/10.1088/2515-7655/ABDC85.
[6] Goujani MJ, Alizadeh M. One-step electrodeposition of Co-Fe electrocatalysts with micro/nano-cauliflower like structure for highly efficient oxygen evolution reaction (OER). J Alloys Compd 2023;960:170557. https://doi.org/10.1016/J.JALLCOM.2023.170557.
[7] Alothman AA, Jabbour K, Manzoor S, Abid AG, Nisa MU, Gomez PH, et al. Facile fabrication of CuScS2/CoO as an efficient electrocatalyst for oxygen evolution reaction and water treatment process. Int J Hydrogen Energy 2024;49:564–79. https://doi.org/10.1016/J.IJHYDENE.2023.08.215.
[8] Kibsgaard J, Chorkendorff I. Considerations for the scaling-up of water splitting catalysts. Nat Energy 2019;4(6):430–3. https://doi.org/10.1038/s41560-019-0407-1. 2019;4.
[9] Lucas S, Haes P. Environmental impacts of extraction and processing of raw materials for the energy transition. 2024.
[10] Jason Z, Song J, Wei C, Huang Z-F, Liu C, Zeng L, et al. A review on fundamentals for designing oxygen evolution electrocatalysts. Chem Soc Rev 2020;49:2196–214. https://doi.org/10.1039/C9CS00607A.
[11] Peng X, Jiang Y, Chen Z, Osman AI, Farghali M, Rooney DW, et al. Recycling municipal, agricultural and industrial waste into energy, fertilizers, food and construction materials, and economic feasibility: a review. Environ Chem Lett 2023;21(2):765–801. https://doi.org/10.1007/S10311-022-01551-5. 2023;21.
[12] The future of food and agriculture Trends and challenges 1. 2013.
[13] Duque-Acevedo M, Belmonte-Ureña LJ, Cortés-García FJ, Camacho-Ferre F. Agricultural waste: review of the evolution, approaches and perspectives on alternative uses. Glob Ecol Conserv 2020;22:e00902. https://doi.org/10.1016/J.GECCO.2020.E00902.
[14] Coleman N, Lovander MD, Leddy J, Gillan EG. Phosphorus-rich metal phosphides: direct and Tin Flux-assisted synthesis and evaluation as hydrogen evolution electrocatalysts. Inorg Chem 2019;58:5013–24. https://doi.org/10.1021/acs.inorgchem.9b00032.
[15] Zhao J, Dong K, Dong X, Shahbaz M. How renewable energy alleviate energy poverty? A global analysis. Renew Energy 2022;186:299–311. https://doi.org/10.1016/J.RENENE.2022.01.005.
[16] COMMITTEE AND THE COMMITTEE OF THE REGIONS Innovating for Sustainable Growth. A Bioeconomy for Europe {SWD. 2012. 11 final} n.d.
[17] Gao G, Hu X, Wang Q, Li C, Chen Q, Zhang L, et al. Functionalization of the biochar from melon seed shell via introducing nitrogen species. J Environ Chem Eng 2023;11:109781. https://doi.org/10.1016/J.JECE.2023.109781.
[18] Guo T, Zhang X, Liu T, Wu Z, Wang DN. K Co-activated biochar-derived molybdenum carbide as efficient electrocatalysts for hydrogen evolution. Appl Surf Sci 2020;509:144879. https://doi.org/10.1016/J.APSUSC.2019.144879.
[19] Rajapaksha AU, Chen SS, Tsang DCW, Zhang M, Vithanage M, Mandal S, et al. Engineered/designer biochar for contaminant removal/immobilization from soil and water: potential and implication of biochar modification. Chemosphere 2016;148:276–91. https://doi.org/10.1016/j.chemosphere.2016.01.043.
[20] Ahmed W, Mehmood S, Mahmood M, Ali S, Shakoor A, Núñez-Delgado A, et al. Adsorption of Pb(II) from wastewater using a red mud modified rice-straw biochar: influencing factors and reusability. Environ Pollut 2023;326:121405. https://doi.org/10.1016/J.ENVPOL.2023.121405.
[21] Dai L, Chang DW, Baek JB, Lu W. Carbon nanomaterials for advanced energy conversion and storage. Small 2012;8:1130–66. https://doi.org/10.1002/SMLL.201101594.
[22] Abdullah H, Ginting RT, Shuwanto H, Kuo DH. Banana peel biowaste-derived carbon composited with Zn(O,S) for solar-light photocatalytic hydrogen generation. Int J Hydrogen Energy 2022;47:41021–33. https://doi.org/10.1016/J.IJHYDENE.2022.09.184.
[23] Atchudan R, Perumal S, Jebakumar Immanuel Edison TN, Aldawood S, Vinodh R, Sundramoorthy AK, et al. Facile synthesis of novel molybdenum disulfide decorated banana peel porous carbon electrode for hydrogen evolution reaction. Chemosphere 2022;307:135712. https://doi.org/10.1016/J.CHEMOSPHERE.2022.135712.
[24] Lofek M, Wojtasik M, Markowski J, Stelmachowski P. Exploring the potential of biochars for boosting electrocatalytic oxygen evolution reaction. Biomass Bioenergy 2025;197:107770. https://doi.org/10.1016/J.BIOMBIOE.2025.107770.
[25] Xia C, Surendran S, Ji S, Kim D, Chae Y, Kim J, et al. A sulfur self-doped multifunctional biochar catalyst for overall water splitting and a supercapacitor from Camellia japonica flowers. Carbon Energy 2022;4:491–505. https://doi.org/10.1002/CEY2.207.
[26] Zhang X, Zhang Q, Cui J, Yan J, Liu J, Wu Y. New insights into the key bifunctional role of sulfur in Fe–N–C single-atom catalysts for ORR/OER. Nanoscale 2022;14:3212–23. https://doi.org/10.1039/D1NR07851H.
[27] Wu Z, Liu R, Wang J, Zhu J, Xiao W, Xuan C, et al. Nitrogen and sulfur co-doping of 3D hollow-structured carbon spheres as an efficient and stable metal free catalyst for the oxygen reduction reaction. Nanoscale 2016;8:19086–92. https://doi.org/10.1039/C6NR06817K.
[28] Horikawa T, Sakao N, Sekida T, Hayashi J, Do DD, Katoh M. Preparation of nitrogen-doped porous carbon by ammonia gas treatment and the effects of N-doping on water adsorption. Carbon 2012;50:1833–42. https://doi.org/10.1016/J.CARBON.2011.12.033. N Y.

[29] Hussain SA, Ali S, Islam ZU, Khan M. Low-temperature synthesis of graphite flakes and carbon-based nanomaterials from banana peels using hydrothermal process for photoelectrochemical water-splitting. Physica E Low Dimens Syst Nanostruct 2022; 141:115231. https://doi.org/10.1016/J.PHYSE.2022.115231.
[30] Sreńscek-Nazzal J, Kamińska A, Serafin J, Michalkiewicz B. Chemical activation of banana peel waste-derived biochar using KOH and urea for CO2 capture. Materials 2024;17:872. https://doi.org/10.3390/MA17040872.
[31] Xu Y, Liu S, Wang M, Zhang J, Ding H, Song Y, et al. Thiourea-assisted one-step fabrication of a novel nitrogen and sulfur co-doped biochar from nanocellulose as metal-free catalyst for efficient activation of peroxymonosulfate. J Hazard Mater 2021;416:125796. https://doi.org/10.1016/J.JHAZMAT.2021.125796.
[32] Ma LL, Hu X, Liu WJ, Li HC, Lam PKS, Zeng RJ, et al. Constructing N, P-dually doped biochar materials from biomass wastes for high-performance bifunctional oxygen electrocatalysts. Chemosphere 2021;278:130508. https://doi.org/10.1016/j.chemosphere.2021.130508.
[33] Zhang Y, Chen L, Hou L, Liu X. N-, P-, and O-doped porous carbon as advanced trifunctional metal-free electrocatalysts. Catal Sci Technol 2023;13:910–6. https://doi.org/10.1039/D2CY01789J.
[34] Torres-Pinto A, Díez AM, Silva CG, Faria JL, Sanromán MÁ, Silva AMT, et al. Tuning graphitic carbon nitride (g-C3N4) electrocatalysts for efficient oxygen evolution reaction (OER). Fuel 2024;360:130575. https://doi.org/10.1016/J.FUEL.2023.130575.
[35] Díez AM, Lyu X, Pazos M, Sanromán MÁ, McCool G, Lebedev OI, et al. Retrofitting of carbon-supported bimetallic Ni-based catalysts by phosphorization for hydrogen evolution reaction in acidic media. Electrochim Acta 2023;443:141923. https://doi.org/10.1016/J.ELECTACTA.2023.141923.
[36] Lazanas AC, Prodromidis MI. Electrochemical impedance Spectroscopy—A tutorial. ACS Meas Sci Au 2023;3:162–93. https://doi.org/10.1021/ACSMEASURESCIAU.2C00070/ASSET/IMAGES/LARGE/TG2C00070_0032.JPEG.
[37] Lamy C, Millet P. A critical review on the definitions used to calculate the energy efficiency coefficients of water electrolysis cells working under near ambient temperature conditions. J Power Sources 2020;447:227350. https://doi.org/10.1016/J.JPOWSOUR.2019.227350.
[38] Rosales E, Escudero S, Pazos M, Sanromán MA. Sustainable removal of Cr(VI) by lime peel and pineapple core wastes. Appl Sci 2019;9:1967. https://doi.org/10.3390/app9101967.
[39] Veerakumar P, Hung ST, Hung PQ, Vishnu Priya V. Synthesis of activated porous carbon from red dragon fruit peel waste for highly active catalytic reduction in toxic organic dyes. Catalysts 2023;13:449. https://doi.org/10.3390/CATAL13020449/S1.
[40] Nandi R, Mondal S, Bhattacharya SS, Sahoo P, Mandal J, Bhattacharyya P. Reversing the tide of trouble: harnessing invasive water hyacinth biochar to mitigate groundwater fluoride contamination. Biomass Convers Biorefin 2024: 1–15. https://doi.org/10.1007/S13399-024-06310-W/FIGURES/6.
[41] Torres E. Biosorption: a review of the latest advances. Processes 2020;8:1584. https://doi.org/10.3390/pr8121584.
[42] Escudero-Curiel S, Pazos M, Sanromán A. Facile one-step synthesis of a versatile nitrogen-doped hydrochar from olive oil production waste, "alperujo", for removing pharmaceuticals from wastewater. Environ Poll 2023;330:121751. https://doi.org/10.1016/j.envpol.2023.121751.
[43] Menéndez JA, Illán-Gómez MJ, y León CAL, Radovic LR. On the difference between the isoelectric point and the point of zero charge of carbons. Carbon 1995;33: 1655–7. https://doi.org/10.1016/0008-6223(95)96817-R. N Y.
[44] Larkin PJ. Introduction. Infrared and Raman spectroscopy. Elsevier; 2018. p. 1–5. https://doi.org/10.1016/b978-0-12-804162-8.00001-x.
[45] Taheri M al R, Astaraei AR, Lakzian A, Emami H. The role of biochar and sulfur-modified biochar on soil water content, biochemical properties and millet crop under saline-sodic and calcareous soil. Plant Soil 2023;499:221–36. https://doi.org/10.1007/S11104-023-05912-Z/FIGURES/7.
[46] Jia YF, Xiao B, Thomas KM. Adsorption of metal ions on nitrogen surface functional groups in activated carbons. Langmuir 2002;18:470–8. https://doi.org/10.1021/LA011161Z/ASSET/IMAGES/LARGE/LA011161ZF00015.JPEG.
[47] Leng L, Xu S, Liu R, Yu T, Zhuo X, Leng S, et al. Nitrogen containing functional groups of biochar: an overview. Bioresour Technol 2019;298:122286. https://doi.org/10.1016/j.biortech.2019.122286.
[48] Xu X, Zheng Y, Gao B, Cao X. N-doped biochar synthesized by a facile ball-milling method for enhanced sorption of CO2 and reactive red. Chem Eng J 2019;368: 564–72. https://doi.org/10.1016/j.cej.2019.02.165.
[49] Li X, Duan X, Han C, Fan X, Li Y, Zhang F, et al. Chemical activation of nitrogen and sulfur co-doped graphene as defect-rich carbocatalyst for electrochemical water splitting. Carbon 2019;148:540–9. https://doi.org/10.1016/j.carbon.2019.04.021. N Y.
[50] Jia Y, Zhang L, Du A, Gao G, Chen J, Yan X, et al. Defect graphene as a trifunctional catalyst for electrochemical reactions. Adv Mater 2016;28:9532–8. https://doi.org/10.1002/ADMA.201602912.
[51] Jiang B, Li J, Liu R, Tian Y, Ren Z, Kong Y, et al. Exclusively carbon-based self-supporting electrodes doped with different heteroatoms for overall water splitting in a wide pH range. Int J Hydrogen Energy 2024;51:1314–26. https://doi.org/10.1016/j.ijhydene.2023.11.080.
[52] Lian F, Cui G, Liu Z, Duo L, Zhang G, Xing B. One-step synthesis of a novel N-doped microporous biochar derived from crop straws with high dye adsorption capacity. J Environ Manag 2016;176:61–8. https://doi.org/10.1016/j.jenvman.2016.03.043.
[53] Wang J, Zhao H, Gao Y, Chen D, Chen C, Saccoccio M, et al. Ba0.5Sr0.5Co0.8Fe0.2O3−δ on N-doped mesoporous carbon derived from organic waste as a bi-functional oxygen catalyst. Int J Hydrogen Energy 2016;41: 10744–54. https://doi.org/10.1016/J.IJHYDENE.2016.04.049.
[54] Sun H, Wang Y, Liu S, Ge L, Wang L, Zhu Z, et al. Facile synthesis of nitrogen doped reduced graphene oxide as a superior metal-free catalyst for oxidation. Chem Commun 2013;49:9914–6. https://doi.org/10.1039/C3CC43401J.
[55] Hu C, Liang Q, Yang Y, Peng Q, Luo Z, Dong J, et al. Conductivity-enhanced porous N/P co-doped metal-free carbon significantly enhances oxygen reduction kinetics for aqueous/flexible zinc-air batteries. J Colloid Interface Sci 2023;633:500–10. https://doi.org/10.1016/J.JCIS.2022.11.118.
[56] Huo X, Jia C, Shi S, Teng T, Zhou S, Hua M, et al. One-step synthesis of high-performance N/S Co-doped porous carbon material for environmental remediation. Processes 2022;10:1359. https://doi.org/10.3390/PR10071359/S1.
[57] Reza MT, Andert J, Wirth B, Busch D, Pielert J, Lynam JG, et al. Hydrothermal carbonization of biomass for energy and crop production. Appl Bioenergy 2014;1: 11–29. https://doi.org/10.2478/apbi-2014-0001.
[58] Feng G, Li W, Ye H, Wang T, Liu Y, Jing B, et al. Molten salt-assisted synthesis of a nitrogen-doped biochar catalyst at low temperature for enhanced degradation of acetaminophen. J Mater Chem A Mater 2025;13:2677–89. https://doi.org/10.1039/D4TA07221A.
[59] Zhou Q, Jiang X, Li X, Jia CQ, Jiang W. Preparation of high-yield N-doped biochar from nitrogen-containing phosphate and its effective adsorption for toluene. RSC Adv 2018;8:30171–9. https://doi.org/10.1039/C8RA05714A.
[60] Gómez-Díaz D, Domínguez-Ramos L, Malucelli G, Freire MS, González-Álvarez J, Lazzari M. S/N/O-Enriched carbons from polyacrylonitrile-based block copolymers for selective separation of gas streams. Polymers (Basel) 2024;16:269. https://doi.org/10.3390/POLYM16020269/S1.
[61] Abo Kamar SM, Ibrahim AA, El-Hakam SA, El-Sharkawy EA, Ahmed AI, Adly MS. Architecture of interconnected cubic NiCo2S4 decorated mesoporous carbon with self-doped nitrogen based-hydrogel for high performance hybrid supercapacitor. J Energy Storage 2024;99:113384. https://doi.org/10.1016/J.EST.2024.113384.
[62] Lima RMAP, dos Reis GS, Lassi U, Lima EC, Dotto GL, de Oliveira HP. Sustainable supercapacitors based on polypyrrole-doped activated biochar from wood waste electrodes. C 2023, Vol 9, Page 59 J Carbon Res 2023;9:59. https://doi.org/10.3390/C9020059.
[63] Morales Salas L, Salazar MR, Escobar B. Doped biochar from an invasive plant "Eichhornia crassipes" for the oxygen reduction reaction. Int J Hydrogen Energy 2022;47:30140–6. https://doi.org/10.1016/J.IJHYDENE.2022.06.223.
[64] Yuan X, Zhu B, Feng J, Wang C, Cai X, Qin R. Biomass bone-derived, N/P-doped hierarchical hard carbon for high-energy potassium-ion batteries. Mater Res Bull 2021;139:111282. https://doi.org/10.1016/J.MATERRESBULL.2021.111282.
[65] Zhao Y, Zhang Q, Gong Z, Zhang W, Ren Y, Li Q, et al. Zanthoxylum bungeanum waste-derived high-nitrogen self-doped porous carbons as efficient adsorbents for methylene blue. Molecules 2024;29. https://doi.org/10.3390/MOLECULES29081809.
[66] Zhong W, Lin Z, Feng S, Wang D, Shen S, Zhang Q, et al. Improved oxygen evolution activity of IrO2 by in situ engineering of an ultra-small Ir sphere shell utilizing a pulsed laser. Nanoscale 2019;11:4407–13. https://doi.org/10.1039/C8NR10163A.
[67] Fang YH, Liu ZP. Mechanism and tafel lines of electro-oxidation of water to oxygen on RuO2(110). J Am Chem Soc 2010;132:18214–22. https://doi.org/10.1021/JA1069272/SUPPL_FILE/JA1069272_SI_001.PDF.
[68] González-Ingelmo M, Granda M, Ruiz B, Fuente E, Sierra U, Rocha VG, et al. Proactive effect of algae-based graphene support on the oxygen evolution reaction electrocatalytic activity of NiFe. Materials 2023;16:7641. https://doi.org/10.3390/MA16247641/S1.
[69] Gao K, Wang B, Tao L, Cunning BV, Zhang Z, Wang S, et al. Efficient metal-free electrocatalysts from N-doped carbon nanomaterials: mono-doping and Co-doping. Adv Mater 2019;31:1805121. https://doi.org/10.1002/ADMA.201805121.
[70] Li C, Xie B, Chen J, He J, He Z. Enhancement of nitrogen and sulfur co-doping on the electrocatalytic properties of carbon nanotubes for VO2+/VO2+ redox reaction. RSC Adv 2017;7:13184–90. https://doi.org/10.1039/C6RA27734A.
[71] Zhang L, Niu J, Li M, Xia Z. Catalytic mechanisms of sulfur-doped graphene as efficient oxygen reduction reaction catalysts for fuel cells. J Phys Chem C 2014; 118:3545–53. https://doi.org/10.1021/JP410501U/ASSET/IMAGES/LARGE/JP-2013-10501U_0006.JPEG.
[72] González-Huerta RG, Ramos-Sánchez G, Balbuena PB. Oxygen evolution in Co-doped RuO2 and IrO2: experimental and theoretical insights to diminish electrolysis overpotential. J Power Sources 2014;268:69–76. https://doi.org/10.1016/J.JPOWSOUR.2014.06.029.
[73] Song F, Straten JW, Lin YM, Ding Y, Schlögl R, Heumann S, et al. Binder-free N-functionalized carbon electrodes for oxygen evolution reaction. Chemelectrochem 2023;10:e202201075. https://doi.org/10.1002/CELC.202201075.
[74] Li X, Gao M, Li S, Yang Z, Zhao X, Liu Y. Bio-based mesoporous carbon-modified Co3O4 quantum dots as efficient electrocatalyst for freshwater, seawater and urea oxidation reaction. Mol Catal 2025;570:114678. https://doi.org/10.1016/J.MCAT.2024.114678.
[75] Plevová M, Hnát J, Žitka J, Pavlovec L, Otmar M, Bouzek K. Optimization of the membrane electrode assembly for an alkaline water electrolyser based on the catalyst-coated membrane. J Power Sources 2022;539:231476. https://doi.org/10.1016/J.JPOWSOUR.2022.231476.
[76] Zhang B, Xu K, Fu X, Guan S, Li X, Peng Z. Novel three-dimensional Ni2P-MoS2 heteronanosheet arrays for highly efficient electrochemical overall water splitting. J Alloys Compd 2021;856:158094. https://doi.org/10.1016/J.JALLCOM.2020.158094.
[77] Anita N, Joany RM, Dorothy R, Aslam J, Rajendran S, Subramania A, et al. Linear polarization resistance (LPR) technique for corrosion measurements.

Electrochemical and Analytical Techniques for Sustainable Corrosion Monitoring Adv Chall Opportun 2023:59–80. https://doi.org/10.1016/B978-0-443-15783-7.00005-0.
[78] Prabu N, Saravanan RSA, Kesavan T, Maduraiveeran G, Sasidharan M. An efficient palm waste derived hierarchical porous carbon towards electrocatalytic hydrogen evolution reaction. Carbon 2019;152:188–97. https://doi.org/10.1016/j.carbon.2019.06.016. N Y.
[79] Patel KB, Parmar B, Ravi K, Patidar R, Chaudhari JC, Srivastava DN, et al. Metal-organic framework derived core-shell nanoparticles as high performance bifunctional electrocatalysts for HER and OER. Appl Surf Sci 2023;616:156499. https://doi.org/10.1016/J.APSUSC.2023.156499.
[80] Ghosh A, Mondal M, Nath Manna R, Bhaumik A. Targeted synthesis of a metal-free thiadiazolate based nitrogen and sulfur rich porous organic polymer for an unprecedented hydrogen evolution in the electrochemical water splitting. J Colloid Interface Sci 2024;658:415–24. https://doi.org/10.1016/J.JCIS.2023.12.076.
[81] Domínguez-Alonso R, Sanromán MÁ, Pazos M, Díez AM. Fe-modified porous biochar derived from tea waste as a high-performance catalyst for oxygen evolution reaction in water splitting. Int J Hydrogen Energy 2025;106:353–65. https://doi.org/10.1016/J.IJHYDENE.2025.02.021.
[82] Yu L, Sun S, Li H, Xu ZJ. Effects of catalyst mass loading on electrocatalytic activity: an example of oxygen evolution reaction. Fund Res 2021;1:448–52. https://doi.org/10.1016/J.FMRE.2021.06.006.
[83] Jiang H, Gu J, Zheng X, Liu M, Qiu X, Wang L, et al. Defect-rich and ultrathin N doped carbon nanosheets as advanced trifunctional metal-free electrocatalysts for the ORR, OER and HER. Energy Environ Sci 2019;12:322–33. https://doi.org/10.1039/C8EE03276A.
[84] Gunasooriya GTKK, Norskov JK. Analysis of acid-stable and active oxides for the oxygen evolution reaction. AIChE Annu Meet Conf Proc 2021;2021-November:3778–87. https://doi.org/10.1021/ACSENERGYLETT.0C02030/ASSET/IMAGES/LARGE/NZ0C02030_0007.JPEG.
[85] You B, Sun Y. Innovative strategies for electrocatalytic water splitting. Acc Chem Res 2018;51:1571–80. https://doi.org/10.1021/ACS.ACCOUNTS.8B00002/ASSET/IMAGES/LARGE/AR-2018-00002J_0008.JPEG.
[86] Marquez RA, Espinosa M, Kalokowski E, Son YJ, Kawashima K, Le TV, et al. A guide to electrocatalyst stability using lab-scale alkaline water electrolyzers. ACS Energy Lett 2024;9:547–55. https://doi.org/10.1021/ACSENERGYLETT.3C02758/SUPPL_FILE/NZ3C02758_SI_002.MP4.
[87] García-Dalí S, Quílez-Bermejo J, Castro-Gutiérrez J, Baccile N, Izquierdo MT, Celzard A, et al. Green and easy synthesis of P-doped carbon-based hydrogen evolution reaction electrocatalysts. Carbon 2023;212:118154. https://doi.org/10.1016/J.CARBON.2023.118154. N Y.
[88] Lim A, Kim J, Lee HJ, Kim HJ, Yoo SJ, Jang JH, et al. Low-loading IrO2 supported on Pt for catalysis of PEM water electrolysis and regenerative fuel cells. Appl Catal, B 2020;272:118955. https://doi.org/10.1016/J.APCATB.2020.118955.
[89] Song H, Yu J, Tang Z, Yang B, Lu S. Halogen-doped carbon dots on amorphous cobalt phosphide as robust electrocatalysts for overall water splitting. Adv Energy Mater 2022;12:2102573. https://doi.org/10.1002/AENM.202102573;SUBPAGE:STRING:FULL.
[90] Li F, Wang H, Wang G, Ding M, Ma Q, Xu H, et al. Novel water-splitting electrolyzer design incorporating a gas diffusion electrode and a gel membrane for highly efficient hydrogen production. Langmuir 2024;40:17109–17. https://doi.org/10.1021/ACS.LANGMUIR.4C02126/ASSET/IMAGES/LARGE/LA4C02126_0005.JPEG.
[91] Mutinda SI, Batugedara TN, Brown B, Brock SL. Co2-xRhxP nanoparticles for overall water splitting in basic media: activation by phase-segregation-assisted nanostructuring at the anode. ChemCatChem 2021;13:4111–9. https://doi.org/10.1002/CCTC.202100483.
[92] Li W, Liu Y, Azam A, Liu Y, Yang J, Wang D, et al. Unlocking efficiency: minimizing energy loss in electrocatalysts for water splitting. Adv Mater 2024;36:2404658. https://doi.org/10.1002/ADMA.202404658.
[93] Svengren H, Chamoun M, Grins J, Johnsson M. Water splitting catalysis studied by using real-time faradaic efficiency obtained through coupled electrolysis and mass spectrometry. Chemelectrochem 2018;5:44–50. https://doi.org/10.1002/CELC.201701086;JOURNAL:JOURNAL:21960216;PAGE:STRING:ARTICLE/CHAPTER.
[94] Rafiq M, Huang Z, Pi C, Hu L, Lu F, Huo K, et al. Designing electrocatalysts for high-current-density freshwater/seawater splitting. https://doi.org/10.31635/renewables.023.202300043; 2024.
[95] Liu H, Zhang Y, Li R, Sun X, Désilets S, Abou-Rachid H, et al. Structural and morphological control of aligned nitrogen-doped carbon nanotubes. Carbon 2010;48:1498–507. https://doi.org/10.1016/J.CARBON.2009.12.045. N Y.
[96] Tian C, Liu Z, Wu Y, Lu X, Yang T, Tao X, et al. Natural-cellulose-nanofibril-tailored NiFe nanoparticles for efficient oxygen evolution reaction. Chemelectrochem 2019;6:3303–10. https://doi.org/10.1002/CELC.201900738.
[97] Conde JJ, Chaparro AM, Ferreira-Aparicio P. Understanding the behavior of electrosprayed carbon black-nafion composite layers. Fuel Cells 2018;18:627–39. https://doi.org/10.1002/FUCE.201700218.